University of Szeged

Albert Szent-Györgyi Medical School
Doctoral School of Multidisciplinary Medical Sciences

Flightless-I and *Drosophila* dLRRFIP2 work together to regulate radial growth of the sarcomeres

PhD Thesis

Péter Görög

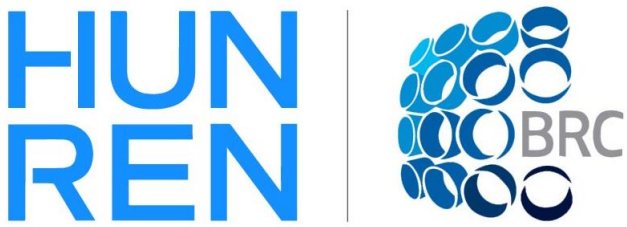

Supervisors:
Dr. József Mihály
Dr. Szilárd Szikora

HUN-REN Biological Research Centre Szeged
Institute of Genetics

Szeged,

2025

Table of contents

1. Publication list

1. Publications related to the thesis

I. **Péter Görög**, Tibor Novák, Tamás F. Polgár, Péter Bíró, Adél Gutheil, Csaba Kozma, Tamás Gajdos, Krisztina Tóth, Alexandra Tóth, Miklós Erdélyi, József Mihály, Szilárd Szikora. Developmental remodelling of Drosophila flight muscle sarcomeres: a scaled myofilament lattice model based on multiscale morphometrics. OPEN BIOLOGY 15 : 250182 (2025)
IF: 3.6 (Q1)

II. Szikora Szilárd; **Görög Péter**; Mihály József. The mechanisms of thin filament assembly and length regulation in muscles. INTERNATIONAL JOURNAL OF MOLECULAR SCIENCES 23 : 10 Paper: 5306 , 25 p. (2022)
IF: 5.6 (Q1)

III. Szikora Szilárd; **Görög Péter**; Kozma Csaba; Mihály József. *Drosophila* models rediscovered with super-resolution microscopy. CELLS 10 : 8 Paper: 1924 , 22 p. (2021)
IF: 7.66 (Q1)

2. Publications not directly related to the thesis

I. István Földi*, Krisztina Tóth*, Rita Gombos, Péter Gaszler, **Péter Görög**, Ioannis Zygouras, Beáta Bugyi, József Mihály. Molecular Dissection of DAAM Function during Axon Growth in *Drosophila* Embryonic Neurons. CELLS 11 : 9 Paper: 1487 , 20 p. (2022)
IF: 6.0 (Q1)

2. Introduction

General description of sarcomere structure

The smallest structural and functional units responsible for muscle contraction are the sarcomeres (Lemke and Schnorrer, 2017; Squire et al., 2005) (Fig. 1). Within these structures the interaction between the two main filamental systems, the actin-based thin filaments and the myosin-based thick filaments generate force by cross-linking and slide pasting each other, ultimately leading to sarcomere shortening and muscle contraction (Huxley and Niedergerke, 1954).

The thick filaments are mainly composed of type II myosin proteins, each consisting of two heavy chains and four light chains (Warrick and Spudich, 1987). The heavy chains feature a C-terminal coiled-coil alpha-helical structure providing structural integrity, and an N-terminal globular head domain capable of binding both ATP and actin (Huxley and Brown, 1967). The head domain also harbors an ATPase activity, which fuels the power stroke of muscle contraction. The two essential and the two regulatory light chains interact with the N-terminal ends of the α-helical tail regions, and they contribute to the modulation of myosin function (Trybus, 1994). The thin filaments are composed of filamentous-actin (F-actin), formed by the polymerization of globular actin (G-actin) monomers. These monomers are arranged in a head-to-tail orientation, giving the F-actin filament a distinct polarity with a (+) end (a.k.a barbed end) and a (-) end (a.k.a. pointed end) (Fletcher and Mullins, 2010). In addition to actin, the thin filaments contain repeating units of tropomyosin and the troponin complex. These regulatory proteins are arranged along the filament and together control the interaction between actin and myosin.

The sarcomeres, bordered by Z-discs, are arranged as serially repeated units along the length of the myofibrils (Fig. 1). The Z-discs serve as anchoring points for the (+) ends of the anti-parallelly oriented actin filaments, which are crosslinked by actin-binding proteins, ensuring the structural integrity of the sarcomere. Additionally, the elastic proteins, such as the vertebrate Titin or the insect Kettin, anchor the thick filaments to the thin filaments at the Z-disc. These proteins act like a spring, providing elasticity to the sarcomeres, which is crucial to prevent overextension and damage during muscle stretching, and they are also essential for muscle relaxation (Granzier and Labeit, 2005; Wang et al., 1979).

The Z-discs are flanked by the myosin-free I-bands that only contain thin filaments, whereas the A-band corresponds to the myosin-containing region, including the actin-myosin overlaps, and the centrally located H-zone, which is devoid of thin filaments and contains the Myosin tail regions of the bipolar thick filaments (Fig. 1). The middle of the H-zone is defined as the M-line, where the thick filaments are crosslinked by myosin-binding proteins (Squire et al., 2005).

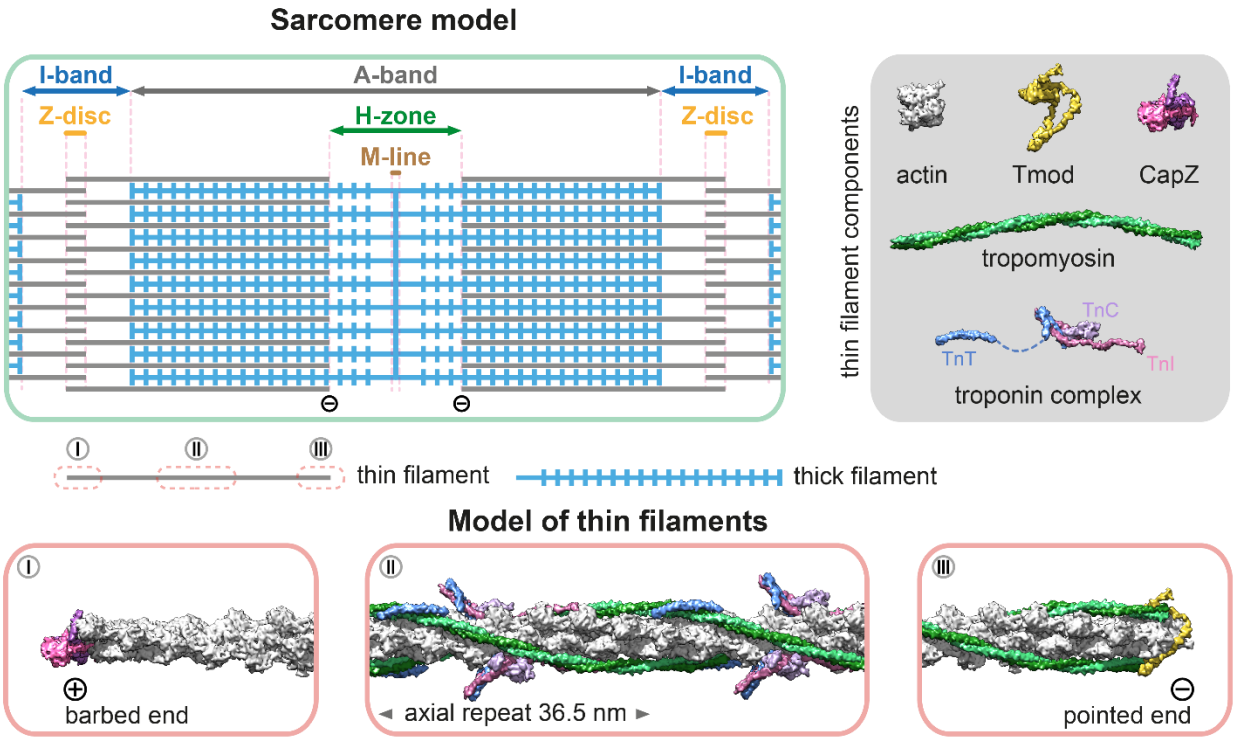

Figure 1. Schematic overview of sarcomere and thin filament architecture. The top left panel shows a simplified sarcomere model with thick (blue) and thin (gray) filaments, as well as key sarcomeric regions. The top right inset (dark gray box) highlights the main components of the thin filament. Molecular models below illustrate three representative regions of the thin filament: (I) the barbed end region, associated with the CapZ complex; (II) the central region, containing tropomyosin–troponin complexes and displaying a full axial repeat; and (III) the pointed end, capped by tropomodulin (Tmod). (adapted from Szikora et al., 2022)

Sarcomere development

Myofibrillogenesis and sarcomere assembly are precisely orchestrated processes that are still subject of active investigations. Despite the numerous gaps in our knowledge, several models have already been proposed to provide a general framework for understanding of these complex processes (Dlugosz et al., 1984; Holtzer et al., 1997; Lu et al., 1992; Rhee et al., 1994; Sanger et al., 2005). Of these, it is presumably the premyofibril model which is the most widely accepted one.

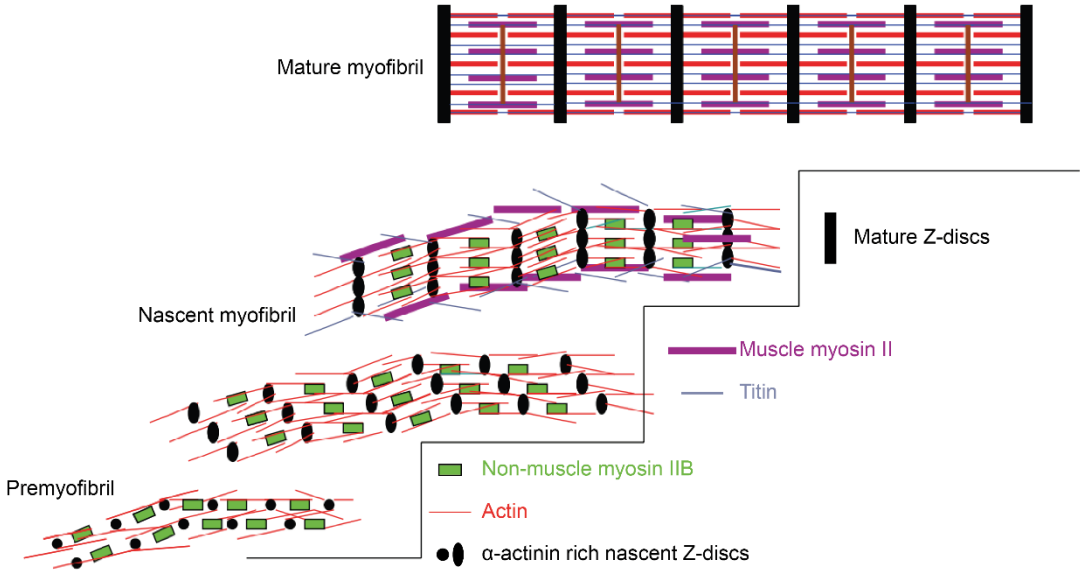

Figure 2. The major steps of myofibrillogenesis based on the premyofibril model. Myofibril assembly initiates with the formation of premyofibrils, which contain minisarcomeres characterized by nascent Z-discs enriched in α-actinin, together with thin filaments (actin, tropomyosin, troponins) and non-muscle myosin II. As premyofibrils align, titin and muscle-specific myosin II are incorporated, giving rise to nascent myofibrils. The subsequent incorporation of additional thin and thick filaments, together with various structural and regulatory proteins, promotes sarcomere elongation and lateral expansion, ultimately leading to the formation of mature sarcomeres at the end of development. (adapted from Stout et al., 2008)

The premyofibril model proposes a stepwise assembly process (Fig. 2). This model suggests that sarcomere formation begins with the emergence of premyofibrils, which are composed of nascent Z-discs, short actin filaments and non-muscle myosin II (Rhee et al., 1994; Stout et al., 2008). The initial steps involve the accumulation of α-actinin, which then crosslinks the actin filaments to form the nascent Z-discs (Jani and Schock, 2007; Katzemich et al., 2013; Passier et al., 2000; Zhou et al., 1999). The non-muscle myosin II present at this stage seems crucial for the initial organization and alignment of the actin filaments. Following the formation of premyofibrils, the next stage involves the integration of key structural and regulatory proteins to further organize and stabilize the Z-discs (Carroll et al., 2004; Carroll et al., 2001; Gonzalez-Morales et al., 2017; Manisastry et al., 2009). After that the elastic proteins start to incorporate into the premyofibril and the non-muscle myosin IIB is exchanged for muscle myosin II, providing elasticity and structural integrity to the formed nascent sarcomeres (sometimes called "proto-sarcomeres") (Chu et al., 2016; Garg et al., 2014; Labeit and Kolmerer, 1995a; Labeit and Kolmerer, 1995b; Moncman and Wang, 1996) (Fig. 2). As development progresses, the proto-sarcomeres grow and mature. This

process involves thin and thick filament addition, as well as incorporation of new proteins, which will further strengthen the structure and function. The precise mechanisms that regulate the two key aspects of this growth process, i.e., the elongation and peripheral addition of the myofilaments, remained largely unknown.

Drosophila model system

Remarkably, the process of muscle contraction and its underlying molecular components are highly conserved across the animal kingdom. The indirect flight muscles (IFM) of *Drosophila melanogaster* exhibit a high similarity to vertebrate skeletal muscles, with well-defined sarcomeres, myofibrils, Z-discs, A-bands and I-bands, as well as thin and thick filament structures. This structural conservation, combined with the precise spatial and temporal resolution of the IFM development, makes *Drosophila* an invaluable model system for studying *in vivo* muscle development and function. Moreover, powerful genetic tools, advanced biochemical approaches and high-resolution imaging techniques are available for *Drosophila* researchers to dissect the molecular mechanisms that govern sarcomere assembly and function, providing insights into both normal muscle physiology and muscle diseases (Lemke and Schnorrer, 2017; Schnorrer et al., 2010; Szikora et al., 2020a).

The development of *Drosophila* IFM involves a series of precisely orchestrated steps that transform nascent myofibrils into the powerful and efficient structures required for flight. At around 36 hours after puparium formation (APF), immature myofibrils begin to emerge within the developing IFM (Reedy and Beall, 1993; Spletter et al., 2018). These structures initially occupy the central region of the thorax and contain proto-sarcomeres, the precursors to mature sarcomeres (Weitkunat et al., 2014). The emergence of the proto-sarcomeres marks the beginning of myofibrillogenesis, a dynamic process characterized by significant changes in myofibril length and thickness (Spletter et al., 2018). This growth continues until approximately 24 hours after eclosion (AE), and the end result of this process is a 1.7-fold increase in sarcomere length and a nearly fivefold increase in thickness (Spletter et al., 2018).

Thin filaments and associated proteins

Actin filaments form the backbone of the sarcomeric thin filaments and are essential for muscle contraction. *In vitro*, actin polymerization follows a well characterized three phase process:

a slow nucleation phase where a few G-actin monomers associate to form a nucleation seed, a rapid elongation phase where monomers are added to both ends of the growing filament, and a steady-state phase where polymerization and depolymerization reach equilibrium (Fig. 3). The filament ends exhibit distinct dynamics due to differing critical concentrations, approximately 0.1 μM at the barbed end and 0.7 μM at the pointed end, resulting in significantly faster growth at the barbed end (Pollard and Borisy, 2003).

However, *in vivo* filament dynamics is more complex, especially in muscle cells, where mechanical demands and developmental programs require precise regulation. The cellular pool of G-actin is tightly controlled through interaction with monomer binding proteins like profilin and thymosin-β4 (Fig. 3). Thymosin-β4 sequesters actin monomers completely, preventing both nucleation and elongation, whereas profilin selectively inhibits pointed end elongation but allows barbed end growth by facilitating actin delivery to polymerizing sites (Carlier and Pantaloni, 1997). Although both profilin and thymosin-β4 are expressed in muscle tissues (Babcock and Rubenstein, 1993; Nagaoka et al., 1996), their contributions to thin filament assembly and elongation have remained mostly uncharacterized. However, a study showed that overexpression of profilin in Drosophila flight muscles induced elongation of thin filaments and sarcomeres (Kooij et al., 2016), indicating a potential role in promoting thin filament formation. Within sarcomeres, thin filaments are uniformly oriented, as their barbed ends are embedded in the Z-disc, while their pointed ends extend toward the M-line (Squire et al., 2005; Szikora et al., 2022). This polarity is maintained and stabilized by capping proteins. CapZ, a heterodimeric complex, binds to the barbed end at the Z-disc and prevents filament elongation at this site (Schafer et al., 1995) (Fig. 3). At the pointed end, Tropomodulin (Tmod) binds and blocks further polymerization or depolymerization (Littlefield et al., 2001), helping to maintain filament length and stability.

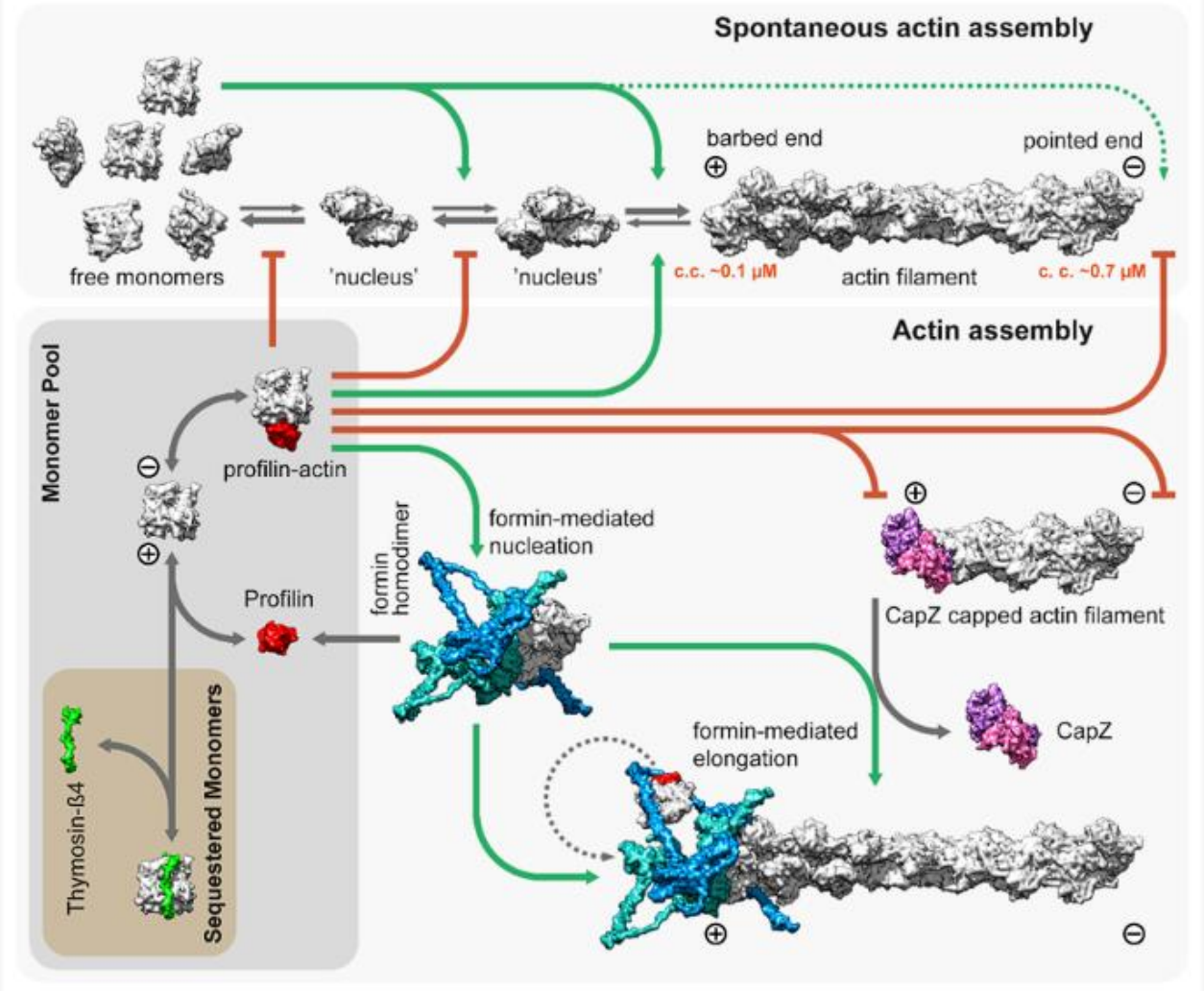

Figure 3. Spontaneous and regulated assembly of actin filaments. Free G-actin monomers can assemble into nucleation seeds, which elongate from both the barbed and pointed ends of the filament. Due to the lower critical concentration at the barbed end, elongation is significantly faster at this site. *In vivo*, actin assembly is tightly regulated by monomer-binding proteins. Thymosin-β4 sequesters G-actin and prevents uncontrolled polymerization, while profilin binds to actin monomers and inhibits spontaneous nucleation and pointed end elongation, yet facilitates barbed end growth by delivering monomers to formins. Formins, such as DAAM1, serve as nucleation and elongation factors and remain associated with the barbed end to support processive filament growth. The structural model of DAAM1 is shown based on a template constructed from multiple known PDB structures. CapZ is depicted bound to the barbed end of the filament, acting as a capping protein that blocks further elongation at this site. (adopted from Szikora et al., 2022)

Despite this tight regulation, thin filaments are not static structures. During muscle development and remodeling, sarcomeric actin filaments can elongate, and interestingly, this growth occurs predominantly at the pointed end, opposite to the direction typically observed in non-muscle cells (Littlefield and Fowler, 2008; Molnar et al., 2014). This suggests that specific

muscle factors allow or promote pointed end assembly under physiological conditions. A key mechanism underlying thin filament length regulation involves a dynamic balance between capping and nucleating activities at the pointed end. Tmod functions as a capping protein, inhibiting actin polymerization and thereby stabilizing filament length. In contrast, Leiomodin (Lmod), a structurally related protein, promotes elongation at the pointed end. The interplay between Tmod and Lmod provides a controlled system for regulating filament extension, allowing fine-tuned remodeling of sarcomere architecture (Tsukada et al., 2010; Yuen et al., 2014). In addition to these pointed-end regulators, formins represent another critical class of actin assembly factors. These multidomain proteins are best known for their role at the barbed end, where the FH1 domain recruits profilin-actin complexes and the FH2 domain promotes elongation while protecting the filament from capping (Chesarone et al., 2010). However, it was also suggested that formins may also contribute to pointed-end dynamics by nucleating short F-actin fragments that are then fused with the pointed end of the growing thin filaments (Molnar et al., 2014). Through such indirect mechanisms, formins may cooperate with Lmod and modulate actin turnover near sites of filament incorporation, playing a more versatile role in sarcomere assembly than previously appreciated.

Whereas regulation of the actin-myosin interaction is revealed at near-atomic resolution, we know much less about the molecular mechanisms of sarcomere growth, including the remarkable lengthening and thickening of the sarcomeres/myofibrils during development. Although it has been shown that, unlike their non-muscle cell counterparts, the sarcomeric actin filaments predominantly grow from their (-) ends (Littlefield and Fowler, 2008; Molnar et al., 2014), the mechanisms of this pointed end elongation remained elusive. As to peripheral growth/radial incorporation of new actin filaments into the sarcomeres, ZASP (Z-band alternatively spliced PDZ-motif) proteins were shown to play a key role (Gonzalez-Morales et al., 2019). However, much needs to be learnt to fully elucidate this process, and further research, aimed at identifying and characterizing the factors involved in sarcomeric actin filament development, will absolutely be necessary for a comprehensive understanding of muscle growth and function.

The actin bindig Flightless-I protein is important for sarcomere development

Flightless-I (FliI), a highly conserved member of the gelsolin superfamily of actin-remodeling proteins, has emerged as a protein of interest due to its potential role in muscle development and function (Deak et al., 1982; Kuwabara et al., 2023; Ruijmbeek et al., 2023). Loss

of FliI has been demonstrated to be fatal during embryonic development in mice and zebrafish (Campbell et al., 2002; Naganawa and Hirata, 2011), and results in abnormal cellularization and gastrulation, leading to death in *Drosophila* (Miklos and De Couet, 1990; Perrimon et al., 1989). Studies across various species have linked *fliI* mutations to muscle related defects, such as in human and mice where *fliI* mutations lead to cardiomyopathy (Al-Hassnan et al., 2020; Kuwabara et al., 2023; Lipov et al., 2023; Ruijmbeek et al., 2023). In zebrafish, reduced *fliI* function results in disorganized skeletal muscle fibers (Granato et al., 1996; Naganawa and Hirata, 2011), and similarly, it was shown in *Drosophila* that reduced activity of FliI disrupts IFM structure and impairs flight ability (Campbell et al., 1993; Deak et al., 1982; Deng et al., 2021; Miklos and De Couet, 1990; Schnorrer et al., 2010).

As member of the gelsolin super-family, FliI comprises of six gelsolin-like domains, located in the C-terminal half of the protein, and in addition, it also contains a leucine-rich repeat (LRR) region (with 15 LRRs) in the N-terminal half. FliI was shown to be able to bind actin monomers and filaments through its gelsolin homology (GH) domains, interestingly however, unlike the canonical Gelsolin proteins, the actin binding ability of FliI is not regulated by calcium, presumably because the calcium binding sites are missing from the GH domains. Conflicting data exist as to whether FliI exhibits a filament-severing activity (Goshima et al., 1999; Liu and Yin, 1998; Mohammad et al., 2012). Based on the loss of function phenotype it was proposed that FliI severs actin filaments during flight muscle development and maintenance, which results in smaller, unfunctional sarcomeres (Deng et al., 2021). However, *in vitro* studies demonstrated that neither the mouse nor the *Drosophila* FliI protein possesses the ability to sever F-actin, instead, FliI behaves as a (+) end binding protein in *in vitro* settings (Mohammad et al., 2012; Pinter et al., 2020). Studies have localized FliI to various subcellular compartments, including the cytoplasm, nucleus, and importantly, at the Z-disc of sarcomeres. The Z-disc, a critical structure that anchors the thin filaments and maintains sarcomere integrity, also serves as a node for force transmission during muscle contraction. The presence of FliI at this crucial junction raises intriguing questions about its potential involvement in sarcomere architecture and contractile function.

3. Objectives

Sarcomere development is a fairly complex process, involving the formation of the pre-myofibrils consisting of proto-sarcomeres, followed by their maturation and growth. Despite ongoing research in this area, our understanding of this process, particularly from the perspective of actin filament dynamics and regulation, remains incomplete. The lack of this knowledge hinders our ability to fully comprehend muscle development disorders and develop effective therapies for muscle diseases. To study this process, we chose *Drosophila* IFM as our primary model system. The IFM, with its highly ordered sarcomere structure and genetic tractability, provides an excellent platform for investigating the molecular mechanisms of sarcomere development. Since there was no comprehensive research as to the developmental dynamics of myofibril growth, first, we wanted to provide a multi-scale characterization of the structural changes during development in a wild-type background to serve as a baseline for our future studies.

In addition, because the human *fliI* gene has recently been linked to childhood-onset cardiomyopathy and cardiac remodeling, we wanted to revisit the function of this protein in IFM development, with the hope that a better characterization of its molecular mechanisms is helpful to understand human disease as well. To address this, we wanted to focus our research on the following questions:

- Is FliI essential for proto-sarcomere assembly, sarcomere maturation, or both? At what specific stages of IFM development is FliI required?
- Where is FliI localized within the sarcomere?
- What are the molecular mechanisms by which FliI influences sarcomere development? What are the interaction partners of FliI?

4. Materials and methods

Drosophila stocks and husbandry

Flies were raised on cornmeal medium and maintained at 25°C under standard laboratory conditions. For the analysis of sarcomere development the w^{1118} strain was used as control and all the knockdown experiments were performed using *y w; mef2-Gal4* (BDSC #27390). In addition, the following stocks were used: *UAS-Act88F::GFP* (BDSC #9253) (Roper et al., 2005) , *duf-Gal4* (Menon and Chia, 2001) *fln-Gal4* (Bryantsev et al., 2012) , $fliI^{3}$ (BDSC #4730), y^{1} $fliI^{8}$ (Kyoto #101241), y^{1} *W* TI(CRIMIC.TG4.0)fliI*$^{CR00462\text{-}TG4.0}$*/FM7h* (designated as *fliICRIMIC.TG4*, BDSC #79264), y^{1} v^{1}*; P{TRIP.JF02720}attP2* (designated as *fliI-TRIP*, BDSC #27566), *P{KK101150}VIE-260B* (designated as *dLRRFIP2KK*, VDRC v110146), W^{1118}*, P{GD13973}v35968* (designated as dLRRFIP2*GD*, VDRC v35968). For staging, white pre-pupae or freshly hatched flies were collected and maintained until they reached the desired age.

The rescue experiments were carried out at 25°C under standard laboratory conditions. Because the *fliI* gene is located on the X chromosome, for the viability assay third instar male larvae were collected with the appropriate genotype, and transferred to a fresh vial for aging. We have monitored the number of individuals that survived till the pupa and adult stages.

Flight assay

Flight tests were carried out with one day old flies. Flies in a group of 5 were released in the middle of a perspex box illuminated from above. Based on their ability to fly, we divided them into 3 categories: fly up (Good Flyer), horizontally (Weak Flyer) or down (Non Flyer). Flies falling to the bottom of the box were counted as flightless.

Muscle preparation and immunostaining

Individual myofibrils were isolated from the IFM using a modified protocol based on Burkart et al. (2007). Briefly, bisected thoraces (hemithoraces) were incubated on ice in relaxing solution (100 mM NaCl, 20 mM NaPi, pH, 7.0, 5 mM $MgCl_2$, 5 mM EGTA, and 5 mM ATP) containing 50% glycerol for 2 hours. The Dorsal Longitudinal Muscles and/or Dorso-Ventral Muscles fibers were then carefully dissected from the hemithoraces and dissociated in an Eppendorf tube by pipetting with 0.5% Triton X-100. The dissociated myofibrils were centrifuged at 10,000 × *g* for 2 minutes at 4°C, and the pellet was re-suspended in 200 µl of relaxing solution

by pipetting. This centrifugation and washing process was repeated twice. After the final centrifugation, the fibers were re-suspended in relaxing solution, and 20 µl of the suspension was placed on a glass coverslip and fixed for 20 minutes either with 4% paraformaldehyde (Thermo Fisher Scientific; paraformaldehyde, 16%, catalog number: 043368.9M) in relaxing solution. See Szikora et al., 2021 for more details. Standard immunohistochemistry procedures were then applied to the samples.

Hemithoraces were dissected from adult flies ~24 hours after eclosion (AE). Bisected thoraces were incubated in 4% paraformaldehyde (Thermo Fisher Scientific; paraformaldehyde, 16%, catalog number: 043368.9M) in relaxing solution for 15 minutes. After the incubation, the muscle was washed twice in a relaxing solution and cut in half at the longitudinal medline. Standard immunohistochemistry procedures were then applied to the sections.

For thoraces transversal sectioning thoraces were separated from the heads and abdomens using fine forceps, with the heads and abdomens discarded. The isolated thoraces were immediately placed in 4% paraformaldehyde (Thermo Fisher Scientific; paraformaldehyde, 16%, catalog number: 043368.9M) in relaxing solution (100 mM NaCl, 20 mM NaPi at pH 7.0, 5 mM MgCl2, 5 mM EGTA, and 5 mM ATP) and fixed overnight at 4°C. After a brief rinse in PBS, the thoraces were submerged in warm 5% agarose ((Lonza, SeaKem LE Agarose) prepared in PBS) and positioned appropriately. Once the agarose had solidified, the blocks were glued to a sample holder and inserted into a vibratome (Microm HM 650 V). To obtain transverse sections of the DLM fibers, the thorax was embedded with its anterior side facing the vibratome blade, positioning the fibers perpendicular to the cutting direction. Using the vibratome, 120 µm thick sections were collected and stored in PBS at 4°C. Standard immunohistochemistry procedures were then applied to the sections

Immunohistochemistry

Fixed tissues were washed three times and blocked in PBS-BT (137 mM NaCl, 2,7 mM KCl, 10 mM Na_2HPO_4, 1,8 mM KH_2PO_4, 0,1% Tween20, 0,2 % BSA, 0,02 % Na-azid) for 2 hours at room temperature (30 minutes for individual myofibril samples). The primary antibodies (Table 1) were applied in blocking solution and incubated overnight at 4°C. After additional washes, secondary antibodies were applied for 2 hours at room temperature. Detection was carried out with highly cross-absorbed goat anti-rabbit, anti-mouse, anti-rat, or anti-chicken IgG secondary antibodies

conjugated to Alexa Fluor 405, Alexa Fluor 488, Alexa Fluor 546, or Alexa Fluor 647 (Life Technologies, 1:600). F-actin was labeled with Alexa Fluor 488-, Alexa Fluor 546-, or Alexa Fluor 647-phalloidin (Life Technologies, Catalog number A12379/ A22283/ A22287, diluted in methanol, 1:200 or 1:800 for dSTORM imaging). After thorough washing, the samples were mounted in antifade reagent (ProLong Gold, P36930; Life Technologies), or stored in PBS until dSTORM imaging.

Protein/Antigen target	Name	Host species	Dilution	Source/Supplier
Primary				
α-Actinin	2G3-3D7	Mouse	1:1000	DSHB
Cpa	Cpa	Rabbit	1:100	Florence Janody (Amandio et al., 2014)
GFP	ab13970	Chicken	1:1000	Abcam
Myosin heavy chain	ab51098	Rat	1:200	Abcam
Flag	F3165-.2MG	Mouse	1:500	Sigma-Aldrich

Table 1. Primary antibody list

Confocal microscopy and image analysis

Confocal images were captured on a Zeiss LSM800 microscope, equipped with a Plan-Apochromat 63x/1.40 OIL DIC M27 or an EC-Plan-Neofluar 10x/0.30 M27 objective.

To measure sarcomere length and moyfibrillum width, 10 individual myofibril containing images were collected, with at least three repetitions. Sarcomere length and diameter were measured directly from raw .czi files using a custom algorithm called Individual Myofibril Analyser (IMA). The source code and a detailed user guide are available online (https://github.com/GorogPeter94/Individual-Myofibril-Analyser-IMA-/tree/main). The presented images were restored using Huygens Professional Software 23.10 (Scientific Volume Imaging). Brightness and contrast were then linearly adjusted in Fiji (Schindelin et al., 2012). Fiber size was measured directly from raw .czi files using the Polygon Selection tool in Fiji to outline each fiber, and the Measure function to determine their size.

Super-resolution dSTROM microscopy

Super-resolution imaging was performed following established protocols (Szikora et al., 2020a; Szikora et al., 2020b). Myofibrils were isolated from the IFM of appropriately staged *Drosophila*. For primary antibody labeling, mouse anti-FLAG M2 (1:500; F3165, Sigma-Aldrich) was used.

Secondary detection was achieved using anti-mouse IgG highly cross-absorbed antibodies conjugated to Alexa Fluor 647 (1:600, Life Technologies). F-actin was labeled with Alexa-488-phalloidin (1:200, Life Technologies). After thorough washing, samples were stored in PBS prior to imaging. dSTORM images were acquired under epi-illumination using a Nikon CFI Apo 100x objective (NA = 1.49) on a custom-built inverted microscope system, based on the Nikon Eclipse Ti-E platform. Illumination was provided by a 647 nm laser (MPB Communications Inc., P_max = 300 mW), controlled via an acousto-optic tunable filter (AOTF), with power set to 2–4 kW/cm² at the sample plane. A secondary 405 nm laser (Nichia, P_max = 60 mW) was employed for reactivation. Imaging was performed using an Andor iXon3 897 BV EMCCD camera (512 × 512 pixels, 16 µm pixel size). Frame stacks were captured with a reduced image size, and a fluorescence filter set (Semrock, LF405/488/561/635-A-000) combined with an additional emission filter (AHF, 690/70 H Bandpass) was used for optimal excitation and emission light separation. The microscope's perfect focus system maintained sample focus with precision <30 nm during imaging. Prior to imaging, the sample storage buffer was exchanged for a GLOX switching buffer (van de Linde et al., 2011), and the sample was mounted onto a microscope slide. Typically, 20,000–50,000 frames were acquired with an exposure time of 20–30 ms per frame. The acquired image stacks were processed and analyzed using the rainSTORM localization software (Rees et al., 2013). Single-molecule images were fitted to a Gaussian point spread function, and their center positions were used to localize the fluorescent molecules. Localizations were filtered based on intensity, precision and standard deviation. Only localizations with precision <20 nm and standard deviation values in the range of $0.8 \leq \sigma \leq 1.0$ were included in the final image reconstruction and subsequent analysis. Drift correction was performed using a correlation-based blind drift correction algorithm to account for mechanical and thermal drift. The spatial coordinates of the localized events were stored, and the final super-resolved image was generated with a pixel size of 10 nm. Structural averaging and distance measurements were conducted using IFM Analyzer v2.1 (https://titan.physx.u-szeged.hu/~adoptim/?page_id=1246).

Transmission electron microscopy

Drosophila hemithoraces (wild type, *fliI*^{8} and *fliI* RNAi) were dissected and fixed in 3.2% paraformaldehyde, 0.5% glutaraldehyde, 1% sucrose, 0.028% $CaCl_2$ in 0.1 M sodium cacodylate (pH 7.4) overnight at 4°C, and washed 2× overnight in 0.1 M sodium cacodylate (pH 7.4) at 4°C.

Samples were postfixed in 1% osmium-tetroxide (Sigma-Aldrich) in distilled water for 1 hr at room temperature. After osmification, samples were briefly rinsed in distilled water for 10 min, then dehydrated using a graded series of ethanol (Molar Chemicals), from 50 to 100% for 10 min in each concentration. Afterwards, muscles were proceeded through propylene oxide (Molar Chemicals), then embedded in the correct orientation in an epoxy-based resin (Durcupan ACM; Sigma-Aldrich). After polymerization for 48 h at 56°C, resin blocks were etched and 50 nm - ultrathin sections were cut using an ultramicrotome (Ultracut UCT, Leica). Sections were mounted on a single-hole, formvar-coated copper grid (Electron Microscopy Sciences), and the contrast of the samples was enhanced by staining with 2% uranyl acetate in 50% ethanol (Molar Chemicals, Electron Microscopy Sciences) and 2% lead citrate in distilled water (Electron Microscopy Sciences). Ultrathin sections were examined with a JEM-1400Flash transmission electron microscope (JEOL). Sections from each animal were systematically screened at low magnification (500–2000×) for the presence of muscle longitudinal and cross sections. Longitudinal and cross sections were recorded with a 2k×2k high-sensitivity scientific complementary metal-oxide-semiconductor camera (Matataki Flash sCMOS, JEOL) as 16-bit grayscale images at an instrumental magnification of 8000× and 20000x, respectively. The quality of TEM images was enhanced by means of ImageJ's Enhance Local Contrast (CLAHE) method.

Simulated IFM image creation

Ground truth images of phalloidin and α-Actinin labeled myofibrils were generated as 2D projections of uniformly labeled cylindrical objects, with overlapping regions representing Z-discs and gaps representing H-zones. These images were scaled and the image formation process was simulated in Fiji (Schindelin et al., 2012). Uneven labeling was modeled by applying a Gaussian noise (sigma = 2). The point spread function (PSF) of the microscope was simulated by convolving the images with a 2D Bessel function (numerical aperture: 1.4, wavelength: 525 nm) using Fiji's MosaicSuite. Shot noise was introduced by adding Poisson noise.

Thick filament spacing calculation

We have carried out the measures similarly as described previously (Chakravorty et al., 2017). We have selected cross-section TEM images with proper filament orientation without contrast enhancement, brightness modification and/or changing image size. With the ImageJ rectangle tool,

an 512×512 pixel size area was copied from the intact region of every myofibrillum, then ImageJ FFT option was used to process the Fourier transform of the images. The distance from the center to the first order reflection was measured in the FFT. For accuracy, we have used the average pixel distance between the reflections. All of this was measured by extracting the histogram along a straight line passing through the center, and then fitting a Gaussian function to each peak to determine the center of the reflections. After that we calculated the distance between these points and averaged it. As there is a strict correlation between the real and the Fourier space it is possible to calculate the real distance from this averaged pixel distance with the following equation: (pixel size of the original TEM image × the total number of pixels of FFT) / calculated average pixel distance) × (2/√3). For example: ((0,819672nm×512pixel)/10.02798pixel) × (2/√3) = 48.32435 nm.

Interaction partner identification with affinity purification coupled to mass spectrometry

Whole thoraces (wild type and *fliI*$^{CRIMIC.TG4}$*;UAS-FLAG::fliI*) were frozen in liquid nitrogen and grounded in lysis buffer (50 mM Tris, 150 mM NaCl, 1% IGEPAL, 1 mM DTT, 3 mM pNpp, 1x protese inhibitor cocktail, 3 mM PMSF) with TissueLyser (Qiagene). Total proteins were extracted as described (Henriqes et al. 2010.). Total protein extracts (4mg/IP) were immunopurified using anti-DYKDDDDK antibody (specific to the Flag-tag) coupled to 50 nm size magnetic beads (MACS® Technology, Miltenyi) with a method modified from (Hubner et al., 2010; Lang et al., 2021) and digested in column with trypsin (Promega). The digestion mixtures were acidified and transferred to a single-use trapping mini-column (Evotip; 1/8 of the samples) and then analyzed with a data-dependent LC-MS/MS method using an Evosep One (LC: 15 SPD; MS1: R :120,000) on-line coupled to a linear ion trap-Orbitrap (Orbitrap-Fusion Lumos, Thermo Fisher Scientific) mass spectrometer operating in positive ion mode. Data acquisition was carried out in data-dependent fashion; multiply charged ions were selected in cycle-time from each MS survey scan for ion-trap HCD fragmentation (MS spectra were acquired in the Orbitrap (R=60000) while MSMS in the ion-trap).

Raw data were converted into peak lists using the in-house Proteome Discoverer (v 1.4) and searched against the Uniprot *Drosophila melanogaster* database using our in-cloud Protein Prospector search engine (v5.15.1) with the following parameters: enzyme: trypsin with maximum 2 missed cleavage; mass accuracies: 10 ppm for precursor ions and 0.6 Da for fragment ions (both

monoisotopic); fixed modification: carbamidomethylation of Cys residues; variable modifications: acetylation of protein N-termini; Met oxidation; Met cleavage; cyclization of N-terminal Gln residues. Acceptance criteria: minimum scores: 22 and 15. 6 IPs (3 wild type, 3 FLAG-fliI) were used for meta analyses. The statistical analyses were performed by edgeR (Robinson et al., 2010) using a modified spectral counting (PSMxCoverage %) to determine relative abundance of individual proteins (Label free quantitation)(Lang et al., 2021). We used a cutoff of P value 0.01 and a Fold Change relative to the negative controls was set to 1.5.

Thin filament length calculation (L_{thin})

$$L_{thin} = \frac{L_{sarcomere}}{2} - \frac{W_{H-zone}}{2} + \frac{W_{Z-disc}}{2}$$

$L_{sarcomere}$ is the average sarcomere length ; W_{H-zone} is the average width of the H-zone; W_{Z-disc} is the average width of the Z-disc

Co-IP

A total of 2 × 10^6 S2 *Drosophila* cultured cells (ATCC CRL-1963) per well were plated onto poly-lysine-coated Labtech chamber slides and transfected with a total of 800ng transfection-grade plasmid DNA using Effectene (Qiagen) according to the manufacturer's instructions. 48 hours after transfection approximately 7 × 10^6 S2 cells were harvested by centrifugation at 1000 × *g* for 2 minutes at 4°C. The cell pellet was then washed with 1 mL of cold PBS and re-centrifuged under the same conditions (1000 × *g* for 2 minutes at 4°C). Subsequently, the pellet was resuspended in 600 µL of FAC buffer (50 mM HEPES, 80 mM KCl, 5 mM $MgCl_2$, 2 mM EGTA, 0.2% Triton X-100, pH 7.4), supplemented with EDTA-free protease inhibitor mixture (Roche catalog number: 04693132001). The suspension was sonicated for 5 seconds to ensure complete lysis. Finally, cellular debris was removed by centrifugation at 12,000 × *g* for 10 minutes at 4°C, and the supernatant containing the cell lysate was transferred to a new Eppendorf tube. For each sample, 15 µL of Anti-FLAG® M2 Magnetic Beads (Sigma; catalog number: M8823-1ML) were used. The beads were then washed twice with 10 times their volume in TBS (25mM Tris-HCl, 150 mM NaCl, adjusted to pH 7.4). After washing, the beads 600 µL of S2 cell lysate was added and incubated with gentle agitation for 2 hours at 4°C. Following incubation, the supernatant was carefully removed. The beads were then washed three times, each time with 1 mL of TBS, allowing

the beads to remain in the wash buffer for 15 minutes per wash. Finally, the bound proteins were eluted by adding 40 µL of 1x SDS loading buffer (300 mM Tris-HCl, 10% SDS, 50% Glycerol, 25% β-mercaptoethanol, 0.05% bromophenol blue) to the beads and incubating the mixture at 100°C for 4 minutes. The resulting eluate, containing immunoprecipitated proteins, was then transferred to a new microcentrifuge tube. Western blots were performed by using standard procedures. Mouse anti-Flag (1:2000, M2, Sigma-Aldrich) and Mouse anti-Myc (1:1000, 9E10: sc-40 Santa Cruz Biotechnology) were used as primary antibodies. Anti-mouse IgG-HRP (light chain specific) (1:10000, 115-035-174 Jackson ImmunoResearch) was used as secondary antibody, and proteins were visualized with the chemiluminescent Millipore Immobilon kit.

GST affinity purification

E. coli SixPack cells (Lipinszki et al., 2018) transformed with the desired pGEX plasmid construct were grown overnight at 37 °C on LB-ampicillin plates. A single colony was used to inoculate 50 mL LB broth auto-induction (AIM) medium (16 g/l tryptone, 10g/l yeast extract, 0.15 g/l $MgSO_4$, 3.3 g/l $(NH_4)2SO_4$, 6.8 g/l KH_2PO_4, 7.1 g/l Na_2HPO_4, 0.5 g/l glucose, 2 g/l alpha lactose) with ampicillin and cultured for 24 h at 37 °C. Cells were harvested (6,000 × *g*, 10 min, 4 °C), and pellets were stored at –70 °C. For purification, 100 µL Glutathione Sepharose bead 4B (Cytiva; catalog number: 17075601) was washed twice with 500µl ice-cold PBS and equilibrated in Basic Lysis Buffer (50 mM Tris-HCl pH 7.5, 5 mM DTT, 50 mM NaCl, 5 mM $MgCl_2$, 10% glycerol, protease inhibitor cocktail (Roche catalog number: 04693132001)). Cell pellets, equivalent to 16 mL culture, were resuspended in 1 ml cold BLB, and sonicated. Inclusion bodies were collected by centrifugation (12,000 × *g*, 10 min, 4 °C). The pellet was resuspended in 640ul BLB followed by addition of 200 µL 10% sarkosyl (2% final concentration). Lysates were sonicated again until they become translucent, then supplemented with 160µl 25% Triton X-100 (4% final concentration) and incubated for 30 min at 4 °C in rotating shaker. After centrifugation (12,000 × *g*, 10 min, 4 °C), cleared supernatants were incubated with pre-equilibrated beads overnight at 4 °C. Beads were washed twice with 1 ml Wash Buffer 1 (50 mM Tris-HCl pH 7.5, 5 mM DTT, 400 mM NaCl, 10% glycerol, 0,5% sarkosyl, 1% Triton-X100) and twice with 1 ml Wash Buffer 2 (50 mM Tris-HCl pH 7.5, 5 mM DTT, 50 mM NaCl, 5 mM $MgCl_2$, 10 mM KCl, 5% glycerol, 0,5% sarkosyl, 1% Triton-X100). Proteins were eluted with 200 µL of 50 mM reduced glutathione in Wash Buffer 2 for 10 min at room temperature. Eluates were analyzed by SDS-PAGE.

Generation of FliI transgenes

The cDNA of FliI was cloned into the pENTR1a vector. This vector was used as a template for generating the L674V transgene (primers listed in Table 2.). The obtained FliI constructs (Full length and L674V) were recombined into the pPFW-attB or pPWF-attB (generated in our laboratory from pPFW and pPWF of the Carnegie Drosophila Gateway Vector Collection, DGRC, Bloomington, IN) vector containing N-terminal or C-terminal Flag-tag in three copies. After sequence verification, the constructs were injected into flies carrying the VIE-260B landing site (60100, VDRC) to create transgenic flies.

Oligonucleotide primer list	
FliI-fwd	5' GATGAGCGTGCTGCCGTTTGT 3'
FliI-rev	5’ GCTCACACAGTGGGCTCGGCA 3’
$FliI^{L674V}$-mutPCR-rev	5' GATCTTTTCCGCCATTACCCTGGCCTTGGAGTTCA 3'
$FliI^{L674V}$-mutPCR-fwd	5' TGAACTCCAAGGCCAGGGTAATGGCGGAAAAGATC 3'

Table 2. Oligonucleotide primers used in this work

Data analysis and Figures

Data collection and organization were carried out in Microsoft Excel, while statistical analysis and graph creation were performed using GraphPad Prism 8 or R. When presenting multiple independent experiments, we used superplots where individual measurements are shown as pooled data points to illustrate spread, distribution, and sample size, while the mean from each experiment is overlaid with error bars to indicate inter-experiment variability. We report sample sizes for both individual measurements and independent experiments. Experiments were considered independent when specimens came from different parental crosses, and each experiment included approximately six animals to capture individual variability. Data normality was assessed using the D’Agostino & Pearson or the Shapiro-Wilk test. The specific statistical tests applied are detailed in the figure legends (ns $P > 0.05$; * $P \leq 0.05$; ** $P \leq 0.01$; *** $P \leq 0.001$; **** $P \leq 0.0001$. Figures were created and finalized in Illustrator (Adobe).

5. Results

During myofibrillogenesis IFM sarcomeres undergo significant, synchronized growth in both length and diameter. However, only a few studies have provided detailed insights into this process (Orfanos et al., 2015; Reedy and Beall, 1993; Spletter et al., 2018). While these studies outline a similar overall pattern of sarcomere growth, a closer look at the data raises several key questions: What is the size of the earliest detectable sarcomeres? Is sarcomere growth a continuous process, or does it includes pauses? When do sarcomeres reach their final size?

Synchronized growth and developmental phases of IFM myofibrillogenesis determined by an automatic evaluation software, Individual Myofibril Analyser

To examine the dynamics of the sarcomere development, we isolated individual myofibrils at twelve developmental time points, spanning from 36 hours APF to 96 hours AE using mixed-sex wild-type flies. We planned to measure sarcomere size, and to ensure accurate measurements, we wanted to test the currently used *in silico* measurement methods. For this test, we created simulated images of IFM myofibrils with known dimensions (Fig. 4A). Firstly, we tested manual measures with ImageJ in a blinded test with four different users (Fig. 4B, C). We observed substantial variability between individuals in myofibril diameter measurements (Fig. 4C, C''), with most significantly underestimating the mean diameter and displaying a high standard deviation relative to the original size (Fig. 4C'). Over the past decade, multiple software solutions have been developed to measure different muscle parameters (Baheux Blin et al., 2024; Neininger-Castro et al., 2023; Spletter et al., 2018; Zhao et al., 2021). However, none achieved the required level of accuracy and efficiency on our dataset, measuring both parameters (Supplementary Table 1). While many utilize widely accessible programming languages, most require programming expertise or still involve manual input for selection, which can be a significant bottleneck in the analysis workflow. Although several of these tools were able to accurately measure sarcomere length, nearly none was able to measure precisely the width of the myofibrils. To address this limitation, we developed a dedicated, user-friendly tool called Individual Myofibril Analyser (IMA), which is a python based automated segmentation and measurement algorithm that enables fast, reliable sarcomere size measurements on individual myofibrils. IMA automatically segments myofibrils from Z-stacks of raw images containing both phalloidin and Z-disc labeling. It uses spline fitting and applies appropriate model functions to intensity profiles to accurately and precisely calculate

both sarcomere length and myofibril width. For sarcomere length, the software records intensity profiles along the myofibrils in the Z-disc marker channel and fits these profiles with multiple Gaussian functions to calculate peak distances, corresponding to sarcomere length. To estimate myofibril diameter, intensity profiles perpendicular to the myofibrils are obtained from the phalloidin channel and fitted with a "disk function" to estimate the diameter more accurately. The accuracy and precision of the tool were validated using our simulated IFM myofibril dataset (Fig 4B, C). In practical applications, the measurements obtained with this software closely matched the ground truth data (4B'', C''). Additionally, it significantly reduced the standard deviation (Fig. 4B', C'), thereby enhancing both the accuracy and precision of the measurements. Moreover, it improved evaluation speed by a factor of 10 to 20.

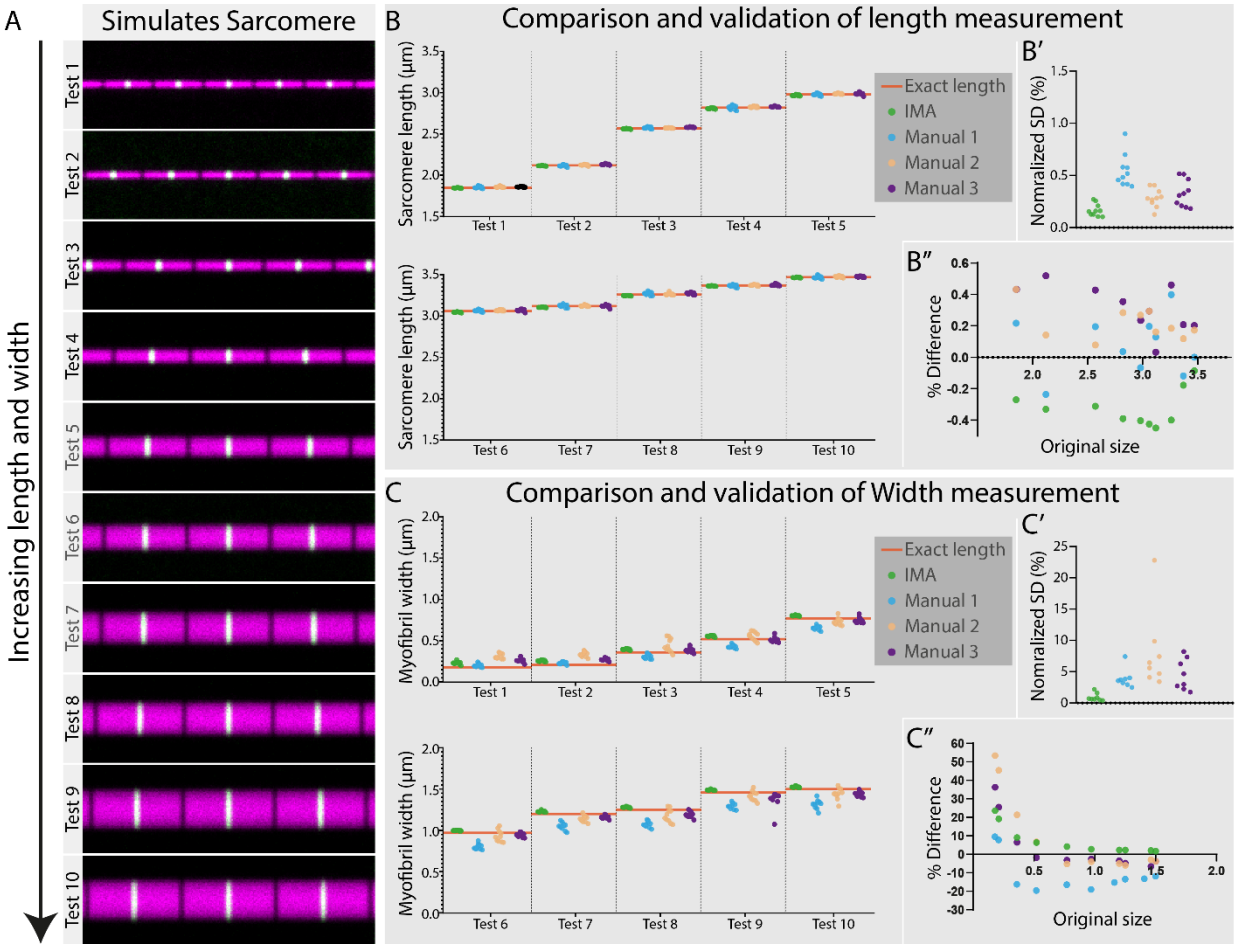

Figure 4. Comparison of sarcomere length and width measurements. (A) Simulated sarcomeres with different length and width from 1-10; (B, C) Comparison of sarcomere length and width measurements obtained using three manual methods and software-based (IMA) analysis; (B', C') Standard deviation of length and width measurements for each simulated dataset (1–10), normalized to the exact sarcomere length; (B'', C'') Percentage deviation of each length and width measurement method from the original (ground truth) values. Colored dots represent individual measurements of sarcomere length and myofibril diameter.

Our developmental analysis indicated that the first immature myofibrils form around 36 hours APF at 25°C. We isolated short, intact individual myofibrils consisting of 4–12 sarcomeres from these young pupae (Fig. 5B), the size of which were comparable to those measured in microdissected intact muscles, confirming their structural integrity. While measuring the width of early myofibrils (36h APF and 48h APF), we also noticed that the measured size is close to the theoretical diffraction limit of conventional fluorescent microscopes (Fig. 5A). Hence, we assumed that these structures could be smaller than we measured originally, therefore to overcome this limitation, we used Airyscan imaging and found that myofibrils are considerably thinner than previously assessed by fluorescent microscopy (Spletter et al., 2018), though still thicker than measured by EM (Reedy and Beall, 1993).

Based on the growth patterns during myofibrillogenesis, we have identified two distinct phases: the organization phase (36-48 hours APF) and the steady growth phase (48 hours APF-24h AE) (Fig. 5A). During the organization phase, sarcomere size remains roughly the same, while the number of sarcomeres per myofibril increases significantly, from around 100 at 36 hours APF to about 230 at 48 hours APF (Spletter et al., 2018). In the steady growth phase few additional sarcomeres are added, resulting in about 270 sarcomeres per myofibril by 60 hours APF (Spletter et al., 2018). During this phase, the sarcomeres exhibited marked growth without significant changes in the assembly rate up to 96 hours APF (Fig. 5A, B). Subsequently, there was a sharp increase in sarcomere length between 96 hours APF and the time of eclosion (0 hours AE), likely due to pre-stretching of the IFM myofibrils as the thoracic exoskeleton expands. Our data showed that sarcomere length and diameter in the IFM generally peak and/or plateau in young adult flies between 12 to 24 hours AE at 25°C (Fig. 5A).

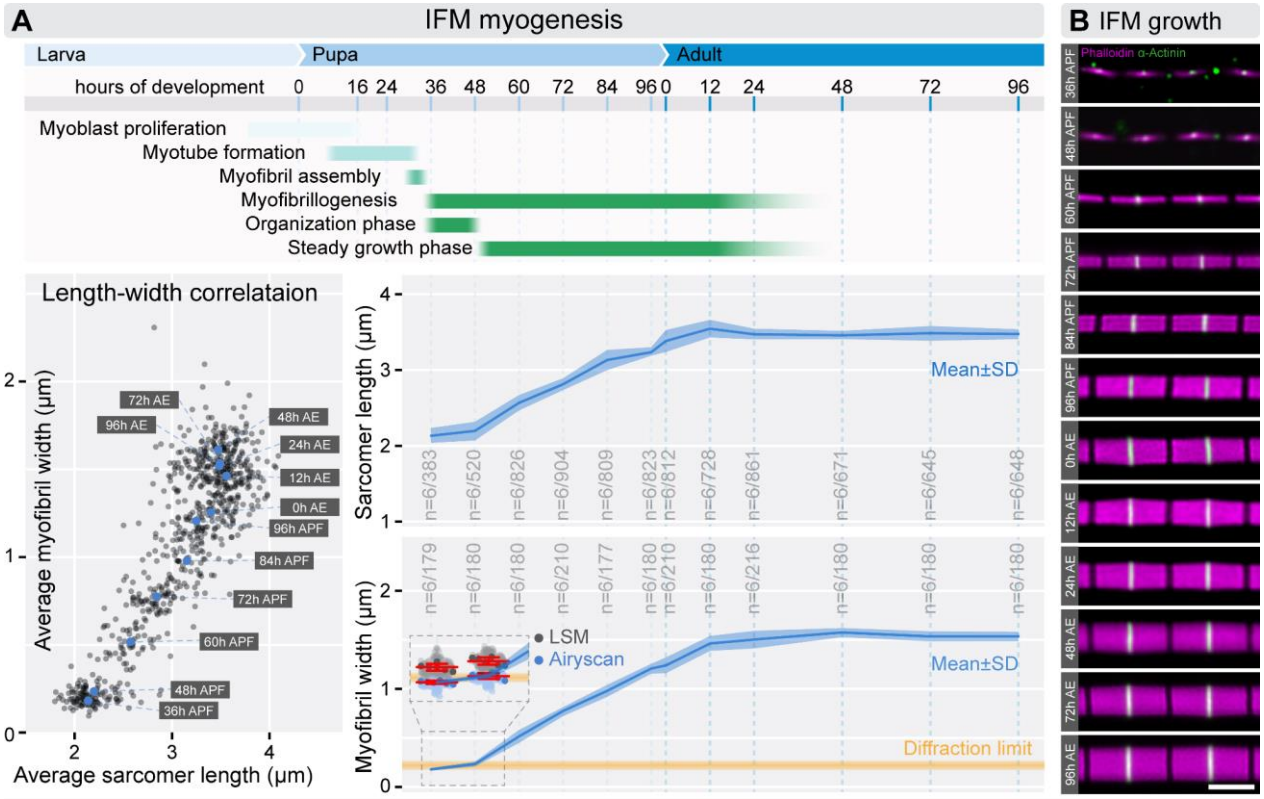

Figure 5. Growth of IFM sarcomeres during myofibrillogenesis. (A) The top panel presents a schematic timeline highlighting key stages of indirect flight muscle (IFM) myogenesis. The bottom left plot shows the correlation between sarcomere length and myofibril width during myofibrillogenesis. Each gray dot represents the mean value from an individual myofibril, while larger blue dots indicate averaged means at specific developmental time points. The plots on the right display average sarcomere length and myofibril width measured across 12 time points, from 36 hours after puparium formation (APF) to 96 hours after eclosion (AE), corresponding to the timeline in the schematic. The number of independent experiments and pooled measurements is indicated by "n". A yellow line marks the theoretical resolution limit of optical microscopy. An inset illustrates that conventional light microscopy (LSM) overestimates early myofibril diameters, whereas Airyscan imaging resolves diameters below the diffraction limit. (B) Representative images of isolated individual myofibrils show sarcomere growth during IFM development. F-actin is stained with phalloidin (magenta), and Z-discs are labeled with α-Actinin (green). Scale bar: 2 µm.

Assessing myofilament assembly and elongation during myofibrillogenesis

During the steady growth phase, the growth of sarcomeres in both length and width involves two different processes: extending the existing myofilaments (thin and thick filaments) and adding new myofilaments at the periphery of the sarcomeres. To investigate the extension of the thin filaments, a pulse-chase experiment was carried out (Fig 6.). Using the *dumbfounded-Gal4* and *flightin-Gal4* driver we expressed GFP-labelled Actin88F monomers and monitored their integration into sarcomeres during myofibrillogenesis with dSTORM microscopy. Labeled actin was incorporated at the periphery of sarcomeres and at the pointed end region of the thin filaments,

forming a "frame" around the “core sarcomere” (Mardahl-Dumesnil and Fowler, 2001; Roper et al., 2005; Shwartz et al., 2016) (Fig 6.). In line with some other studies, these results indicate that thin filaments extend specifically at their (-) ends (Littlefield and Fowler, 2008; Mardahl-Dumesnil and Fowler, 2001; Shwartz et al., 2016). As for radial growth, these images highlighted that newly formed myofilaments integrate at the edges of the sarcomeres, which leads to the gradual expansion of the structure.

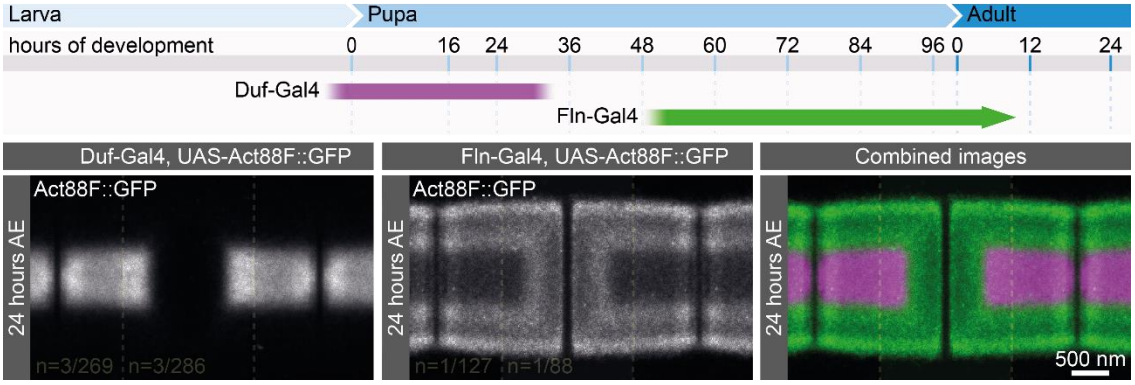

Figure 6. Growth of IFM sarcomeres during myofibrillogenesis. Top: Schematic representation of the temporal expression patterns driven by *duf-Gal4* and *fln-Gal4*. Bottom: dSTORM reconstructions showing the incorporation of GFP-tagged Act88F monomers into IFM myofibrils using the respective Gal4 drivers.

To extend our studies to the level of individual myofilaments, we utilized electron microscopy to count myofilaments across four developmental stages from 36 hours APF to 24 hours AE, and fluorescent nanoscopy to measure myofilament length precisely (Fig. 7). To examine myofilament number and arrangement during myofibrillogenesis, we analyzed cross-sections of DLM myofibrils using transmission electron microscopy (Fig. 7A, A’). At 36 hours APF, myofibrils appeared as disorganized clusters of filaments, with an average of 23 thick filaments per myofibril. By 48 hours APF most myofibrils exhibit a highly ordered structure, with an average of 32 thick filaments arranged in a roughly hexagonal pattern at a 1:3 ratio of thick to thin filaments, though some irregularities are still visible at the edges of these structures (Fig. 7A). At 72 hours APF, the lattice structure became fully organized, resembling the adult form, with an average of 152 thick filaments. In adult flies (24 hours AE), the average number of thick filaments per sarcomere increased to 846, consistent with other studies (Chakravorty et al., 2017; Fernandes and Schock, 2014; Shwartz et al., 2016).

At 36 hours APF, the thin filaments had not yet aligned in perfect register at the Z-disc, with most measuring less than 560 nm in length (Fig. 7B, B’’). The overlap of the thin filaments at

the Z-disc was approximately 240 nm (Fig. 7B'). By 48 hours APF we measured a thin filament array length of ~490 nm (Fig. 7B''), which is somewhat shorter than at 36 hours APF. Nevertheless, we think it very unlikely that the actin filaments indeed shrink; instead, we suspect that by 48 hours APF the sarcomeres attain a higher structural regularity than at 36 hours APF, which makes the apparent length of the thin filament array shorter without significant changes in filament length. Consistent with this idea, by 48 hours APF the Z-discs became more structured, with a reduced thin filament overlap of ~140 nm. At 72 hours APF the thin filament array adopted a structure closely resembling its mature form (Fig. 7A). Thin filaments extended to ~1330 nm (Fig. 7B''), and the overlap at the Z-disc was reduced to ~98 nm, which is only slightly larger than the ~94 nm observed in mature sarcomeres (Fig. 7B'). Finally, by 24 hours AE, thin filaments reached their final length of ~1680 nm, and all Z-disc markers exhibited their fully matured pattern (Szikora et al., 2020a).

Our measurements revealed that during the 90 hours of myofibrillogenesis, the disorganized clusters of filaments progressively organize into highly ordered, periodic sarcomeric structures, reflecting the maturation and alignment of contractile units essential for muscle function. During this process, the length of the thin filaments is increased by 3-folds and the number of thin filaments incorporated into the developing structure rises by approximately 37-fold, highlighting the extensive assembly and organization required for functional sarcomere formation. Our results, in conjunction with previous studies, indicate that this lengthening process takes place primarily at the pointed end of the thin filaments. Beyond elongation of the existing filaments, new myofilaments also form and incorporate at the periphery of the developing myofibrils. This dual mechanism contributes to both longitudinal and radial growth of the sarcomeres, but the mechanisms driving these processes remain largely unclear.

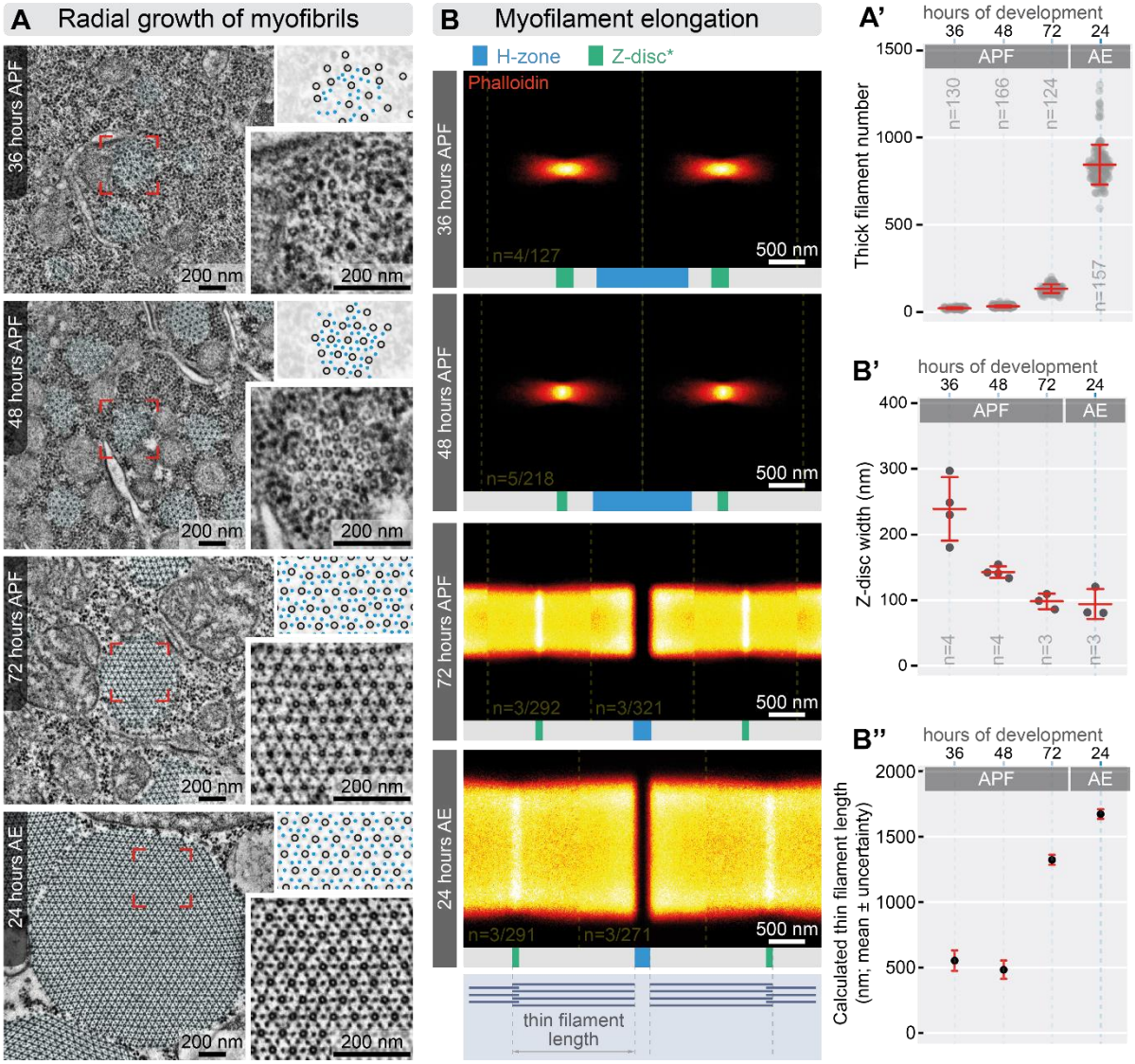

Figure 7. Characterization of myofilament number and length during myofibrillogenesis. (A) TEM cross-sections of DLM fibers highlight radial growth of the myofibrils (highlighted in cyan) throughout myofibrillogenesis. Higher-resolution insets (corresponding to the area marked by red squares) on the right show changes in the lattice organization of the myofilaments (schemes with black circles and blue dots mark position of the thick and thin filaments, respectively). (A') The accompanying plot displays the average number of thick filaments observed in the TEM cross-sections of myofibrils, with the mean and s.d. indicated. (B) Averaged dSTORM reconstructions illustrate the growth and spatial organization of thin filaments (stained with phalloidin, on the left) during myofibrillogenesis. (B'-B'') Plots showing measurements of Z-disc width derived from dSTORM images (B') and the calculated thin filament length (B''). In panels A' and B' light gray dots represent the mean values for individual myofibrils, while dark gray dots indicate the mean values from independent experiments. The mean and s.d. of these experiments are provided. "n" refers to the number of individual measurements.

Flightless regulates sarcomere size and myofibril organization

Whereas former studies identified a few key proteins involved in thin filament elongation, much less was learnt about the mechanisms of and the main players involved in peripheral growth of the sarcomeres. One potentially interesting candidate for such a role is FliI, which was shown to play a role in actin filament dynamics and sarcomere organization. In line with these earlier studies, we found that the muscle-specific knockdown of *fliI* and the hypomorphic *fliI* alleles ($fliI^{3}$ and $fliI^{8}$) lead to abnormalities in IFM organization, ultimately resulting in a complete loss of flight ability (Campbell et al., 1993; Deak et al., 1982; Deng et al., 2021; Miklos and De Couet, 1990; Perrimon et al., 1989; Schnorrer et al., 2010) (Fig. 8A-D'', E). Detailed analysis revealed that the loss of *fliI* causes a number of defects in muscle development, including the formation of prominent myofibrillar aggregates on the surface of the muscle fibers and severe impairments in myofibril formation and organization (Fig. 8B'-D', B''-D''). High-resolution imaging demonstrated that these myofibrils are either severely disrupted or exhibit reduced thickness and shortened sarcomeres as compared to control IFM myofibrils (Deng et al., 2021) (Fig. 9). To quantify these observations, individual myofibrils were isolated for precise measurements, confirming that the RNAi mediated knockdown (KD) of *fliI* results in significantly shorter sarcomeres (2.451 ± 0.316 µm) and thinner myofibrils (0.714 ± 0.09 µm) compared to controls (Fig. 9). The $fliI^{3}$ and $fliI^{8}$ alleles have somewhat milder effects on sarcomere length ($fliI^{3}$: 2.759 ± 0.218 µm; $fliI^{8}$: 2.905 ± 0.308 µm) and myofibril width ($fliI^{3}$: 1.142 ± 0.133 µm; $fliI^{8}$: 0.9796 ± 0.134 µm), but they exhibit the same tendence as observed upon *fliI* KD (Fig. 9).

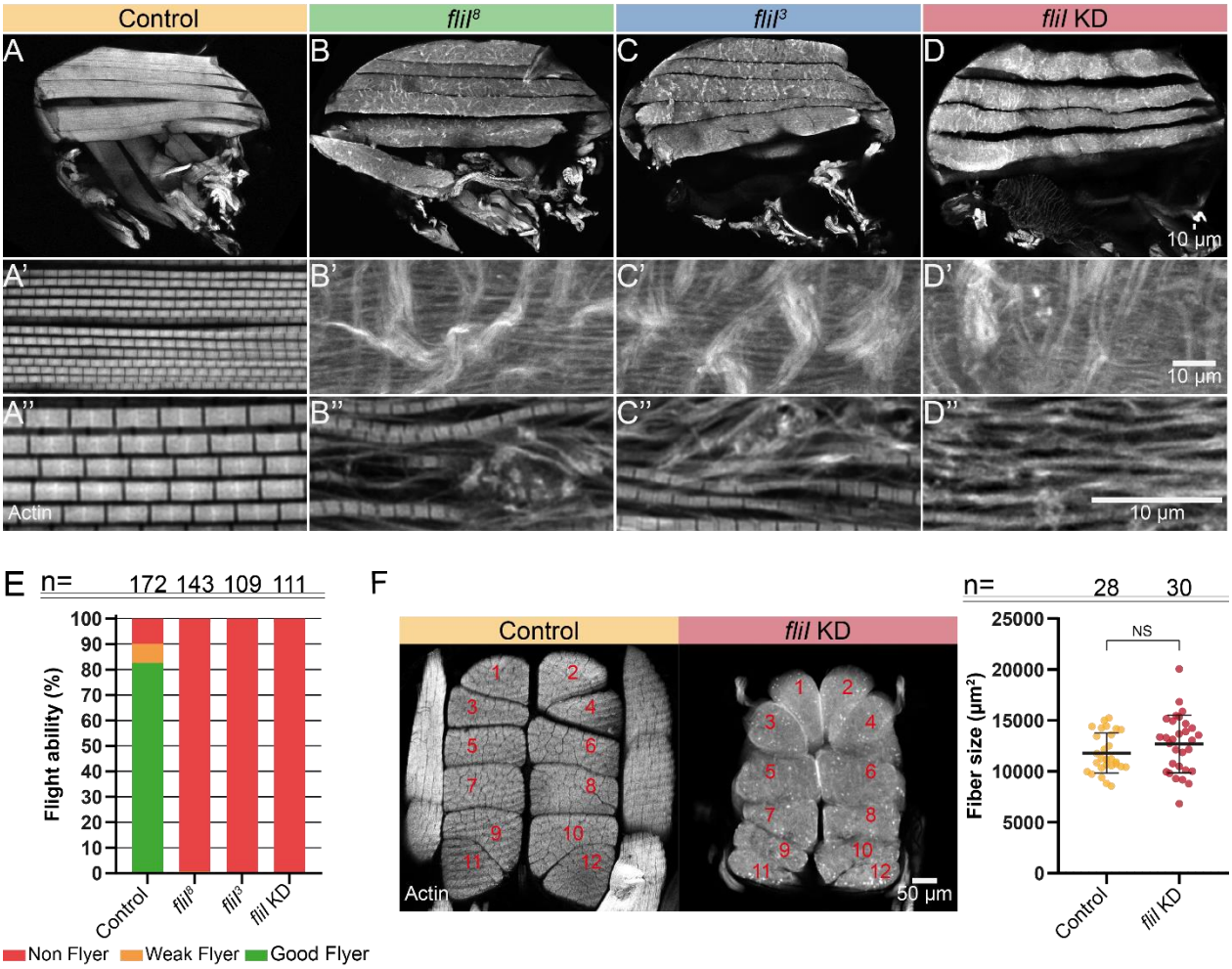

Figure 8. Flightless-I is essential for proper IFM development. (A-D) Microdissected IFMs at 24h AE from *fliI* deficient flies show disrupted muscle architecture and prominent actin aggregates. (A'-D'') Higher magnification images comparing IFM morphology between control and *fliI* deficient flies. (E) Quantification of the flight ability in control, $fliI^{3}$, $fliI^{8}$ and *fliI* KD flies at 24h AE (n indicates the number of flies tested). (F) Transverse vibratome section of the thorax highlighting the 12 dorsal longitudinal muscle (DLM) fibers. The accompanying graph quantifies the area of the 7th and 8th DLM in control and *fliI* knockdown flies at 24h AE. "n" indicates the number of myofiber counted. Statistical analysis was performed using Mann–Whitney test.

These observations demonstrate that FliI plays a specific role in regulating IFM sarcomere structure. However, it may not be essential during the initial phases of flight muscle development, as the flight muscle fibers are present in the expected numbers with properly formed attachment sites, and can achieve close to normal size in *fliI* deficient animals (12689µm2, compared to the 11788µm2 of controls) (Fig. 8F).

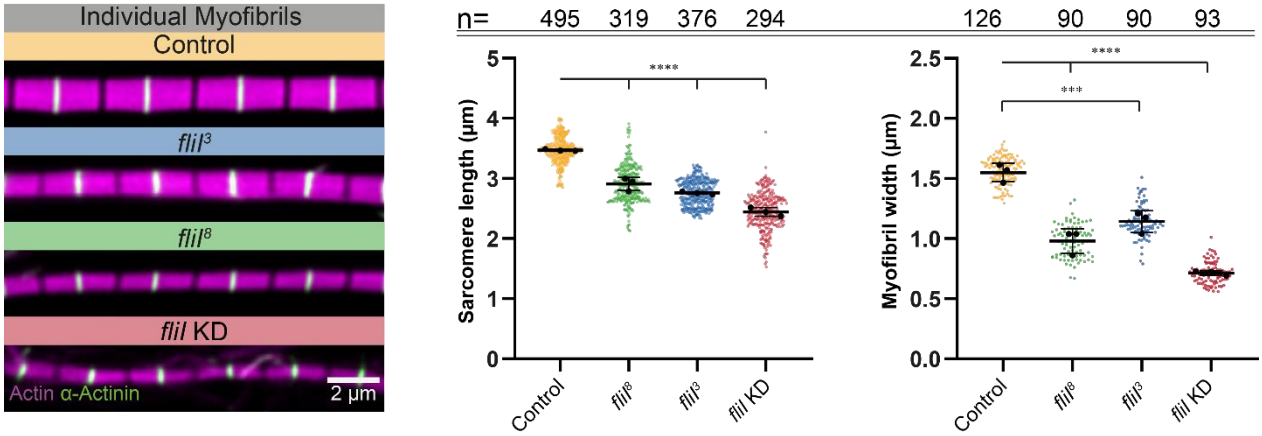

Figure 9. Flightless-I contribute to the length and width regulation. Left: Representative images of sarcomere structure in control, *fliI*^{3}, *fliI*^{8} and *fliI* KD flies at 24h AE, stained with phalloidin and α-actinin to visualize the actin and Z-disc, respectively. Right: Quantification of sarcomere length and width in the same genotypes at 24h AE. Colored dots represent individual measurements of sarcomere length and myofibril diameter, while the larger black dots indicate the mean values from independent experiments. Error bars represent the mean and s.d. of independent experiments. "n" refers to the number of sarcomere measured. Statistical analysis was performed using one-way ANOVA with Tukey's multiple comparison test.

Myofilaments fail to incorporate into myofibrils in *fliI* deficient animals.

To further examine the structural changes in the absence of FliI, we analyzed the ultrastructure of control and *fliI* deficient IFMs (*fliI* KD and *fliI*^{8}) with transmission electron microscopy in young adults (24 hours AE). The electron micrographs of longitudinal and cross-sections of DLM fibers support our earlier findings, clearly displaying significantly shorter and thinner sarcomeres in *fliI* deficient IFMs (Fig. 10, 11). Furthermore, the TEM revealed abnormalities in Z-discs morphology and myofilament organization. In *fliI* mutant muscles, the Z-disc were often smaller and confined to the sarcomere core, while the peripheral myofilaments often displayed loose connections or were completely detached from the core of the myofibrils (Fig. 10).

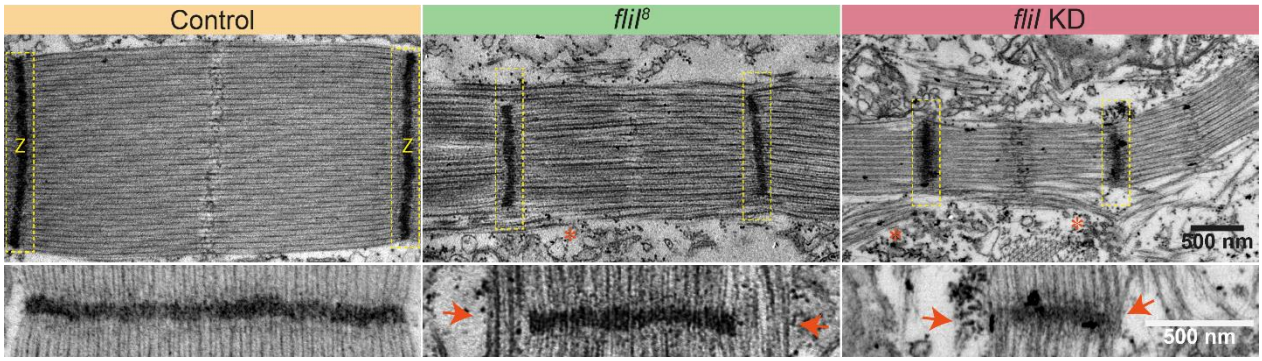

Figure 10. Flightless-I is essential for the proper myofilament integration. Electron micrographs of longitudinal sections from DLM fibers of control, *fliI*^{8} and *fliI* KD flies at 24h AE. Red stars and arrows indicate loosely connected or unintegrated filaments and the Z-disc abnormalities, respectively.

Interestingly, unlike in the peripheral regions, in the central region of the myofibrils the normal 3:1 ratio of thin to thick filaments was maintained, and the spacing within the hexagonal myofilament lattice, as measured by average thick filament distance (control: 48.03nm; *fliI*^{8}: 47.26nm; *UAS-fliI-TRIP*: 46.42nm), appeared unaffected (Fig. 11A). Furthermore, we observed zebra-body-like electron-dense structures (Fig. 11B), which appeared as actin aggregates in the fluorescent images. These structures are usually surrounded by thin filaments, a characteristic also present in *fliI* deficient mouse hearts (Kuwabara et al., 2023) and often associated with myopathies (Lake and Wilson, 1975).

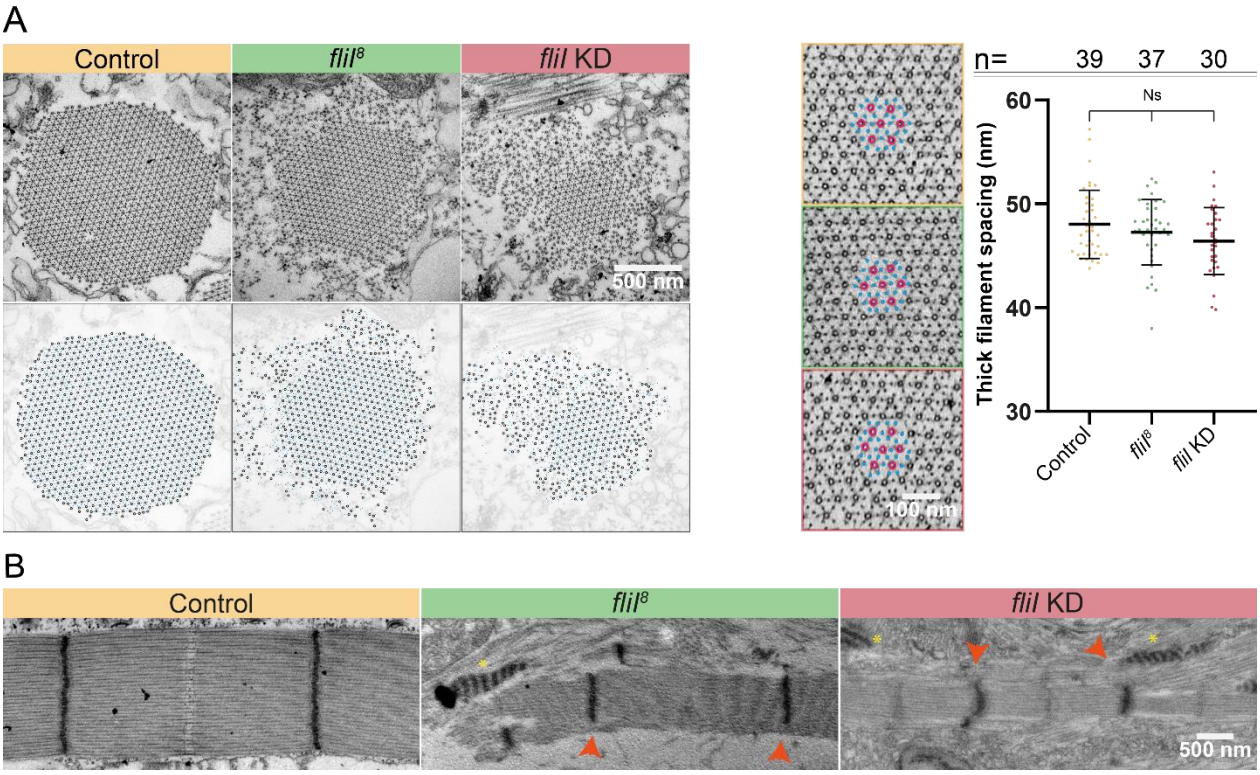

Figure 11. Flightless-I is not essential for myofibril core formation. (A) Left panel: Representative electron micrographs of control, *fliI*^{8} and *fliI* KD cross-sections myofibrils from DLM fibers at 24h AE. Upper panels show raw images; lower panels show the same images annotated with a schematic overlay highlighting the positions of thick (black circles) and thin (blue dots) filaments. Right panel: quantification of thick filament spacing (μm) in the three genotypes. Colored dots represent individual myofibrils; error bars represent the mean and s.d. "n" refers to the number of myofibrils analyzed. Statistical analysis was performed using one-way ANOVA with Tukey's multiple comparison test. (B) Lower-magnification electron micrographs reveal the presence of zebra body-like structures. Red arrows indicate the unintegrated filaments and yellow stars show the zebra-body-like structures.

To analyze the developmental role of FliI further, we examined isolated individual myofibrils from specific phases of myofibrillogenesis using confocal microscope, and examined cross-

sections of DLM fibers with TEM from *fliI* KD samples (Fig. 12). Intriguingly, in the early stages, at 36 hours APF, the loss of FliI did not cause any noticeable defects, while at 48 hours APF the sarcomere ultrastructure appeared identical to the wild type, although the sarcomeres were already shorter. By 72h APF alterations in IFM structure become evident, including unequal sarcomere length and myofibril width (Figure 12A). However, by 96h APF, the myofibrils had the same abnormal appearance as in the adults, with a strong reduction in myofibril diameter and the occurrence of unintegrated filaments in a considerable amount near all myofibrils (Fig. 12A, B).

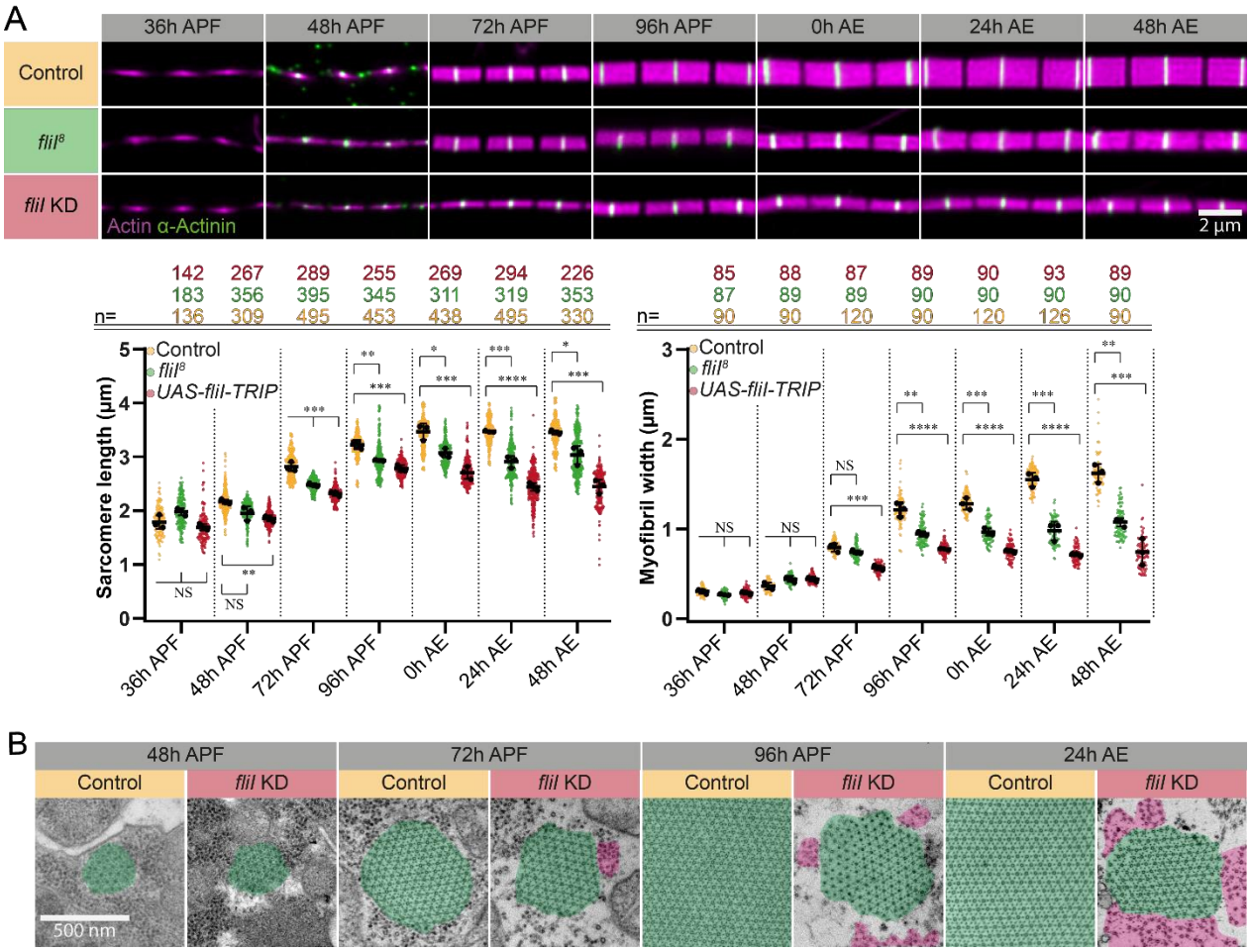

Figure 12. Flightless-I is required during the steady growth phase of myofibrillogenesis. (A) Isolated Individual myofibrils represent the mean size of the sarcomeres at every measured time points. Quantification of sarcomere length and width in control and *fliI* knockdown flies at 7 different time points during the myofibrillogenesis. Colored dots represent individual measurements of sarcomere length and myofibril diameter, while the larger black dots indicate the mean values from independent experiments. Error bars represent the mean and s.d. of independent experiments. "n" refers to the number of sarcomeres measured. Statistical analysis was performed using one-way ANOVA with Tukey's multiple comparison test. (B) Electron micrographs of control, and *fliI* KD cross-sections myofibrils from DLM fibers at specific phases of myofibrillogenesis. Colored areas highlight the organized (green) and unintegrated filaments (magenta).

Taken together, our developmental analysis highlighted that *fliI* does not affect the formation of the premyofibrils/proto-sarcomeres. However, the subsequent elongation of the sarcomeres and radial thickening of the myofibrils are impaired. The presence of "loose" filaments, which first appear between 48h and 72h APF, indicates that formation of the myofilaments is not compromised, but their incorporation into a regular myofibrillar lattice is impaired. Therefore, these observations suggest that FliI is primarily required during the second phase of myofibrillogenesis after all myofibrils and sarcomeres have formed, when it appears to play a specific role in anchoring and organizing the peripheral myofilaments at the Z-disc, also implying that the Z-disc is a critical spatial determinant of radial sarcomere growth.

FliI is enriched at the barbed-end of the thin filaments in developing and mature IFM

To better understand how FliI regulates Z-disc formation and myofibril thickening, we decided to assess its localization in the IFM. Members of FliI protein family consist of an LRR region at its N-terminus and 6 gelsolin-like repeats at their C-terminus (Campbell et al., 1993), and they have been shown to localize to actin-based structures via their gelsolin homology domains in *in vivo* (Davy et al., 2001) and *in vitro* assays (Goshima et al., 1999; Liu and Yin, 1998; Mohammad et al., 2012; Pinter et al., 2020). In vertebrate muscles, the overexpressed wild type FliI is localized in the A-band and it is suggested to decorate the thin filaments (Kuwabara et al., 2023). Regarding the localization of *Drosophila* FliI in the IFM, conflicting data exist in the literature, which most likely stems from the absence of a specific antibody targeting the *Drosophila* protein. Using antibodies raised against the human FliI protein in fruit fly muscles indicated that FliI is present at the M-line and the Z-discs (Schnorrer et al., 2010; Szikora et al., 2020a), whereas a later study only detected FliI in the Z-discs of mature IFM (Deng et al., 2021).

To revisit the localization of FliI we applied a genetic approach, in which we expressed a FLAG-tagged version of the full-length FliI protein in a *fliI* protein-null mutant background ($fliI^{CRIMIC.TG4}$). The CRIMIC.TG4 cassette expresses GAL4 under the control of the endogenous *fliI* promoter while simultaneously halting transcription at the 3' end of the GAL4 (Lee et al., 2018), which leads to the production of a non-functional, truncated FliI and a GAL4 protein. This approach allowed us to track FliI localization using FLAG::FliI and FliI::FLAG transgenes (Fig. 13A).

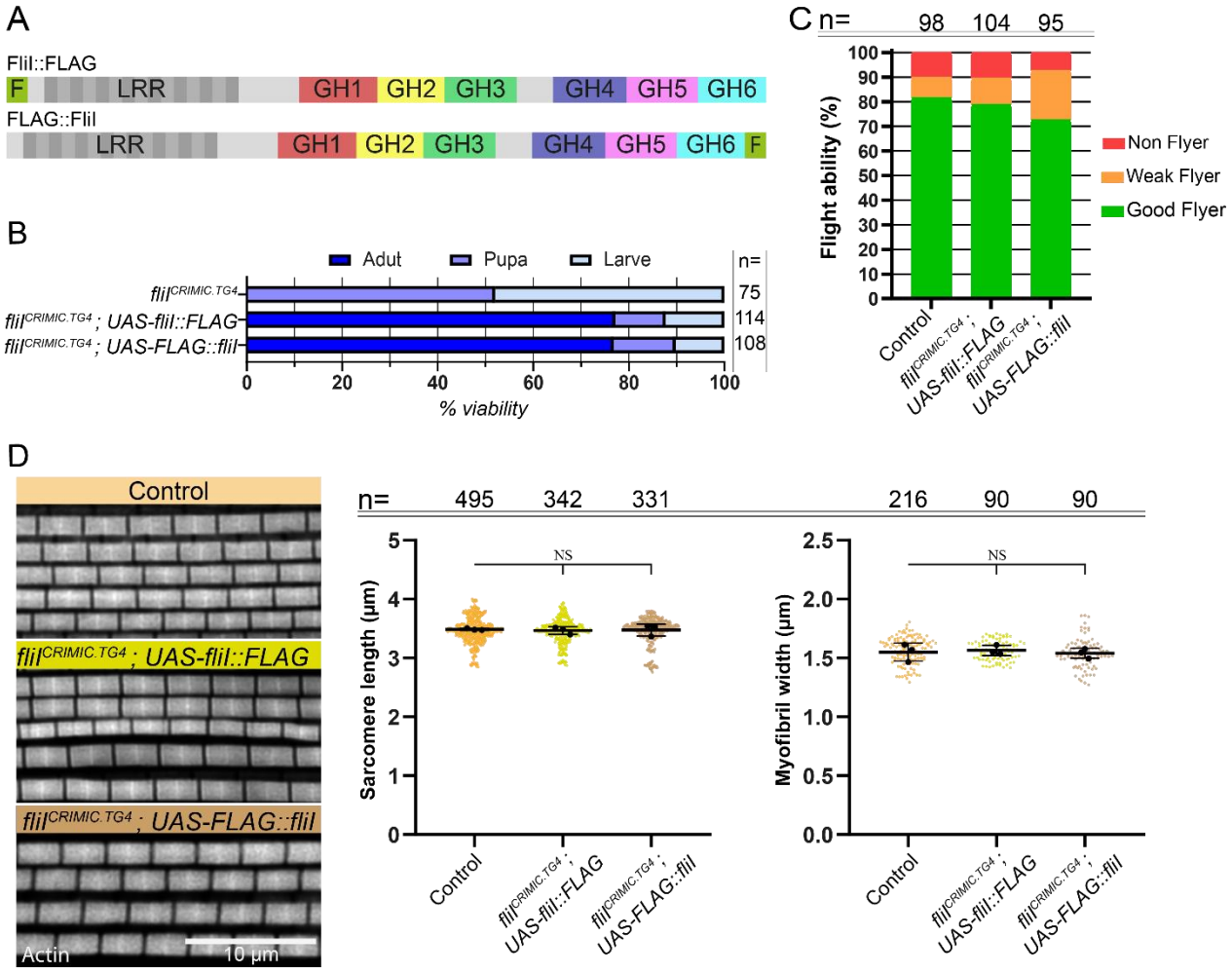

Figure 13. FLAG-tagged FliI proteins are able to rescue lethality and flight ability. (A) Schematic representation of the N- and C-terminal Flag-tagged FliI protein. (B) The graph representing the viability (% survival) of flies in the Flightless (FliI) null background, with or without rescue by C- or N-terminally tagged FliI expressed using the CRIMIC-Gal4 driver. “n” indicates the number of larvae collected and tested. (C) The graph on the right shows the quantification of the flight ability in control and rescued flies at 24h AE. “n” indicates the number of flies tested. (D) High-resolution IFM myofibrils image of control and FliI rescue animals. The plots represent a quantitative analysis of sarcomere length and width. Colored dots represent individual measurements of sarcomere length and myofibril diameter, while the larger black dots indicate the mean values from independent experiments. Error bars represent the mean and s.d. of independent experiments. "n" refers to the number of sarcomeres measured. Statistical analysis was performed using one-way ANOVA with Tukey’s multiple comparison test.

However, before doing so, we first tested whether the tagged proteins are functional in rescue experiments. Hemizygous males carrying the *fliI*$^{CRIMIC.TG4}$ protein null allele die either during the larval stage (52%) or the early pupal stage (48%) (Fig. 13B). However, the lethal phenotype of these flies can be rescued in approximately 77% of the offspring to adulthood by expression of the full-length UAS-FliI transgenes having FLAG tags either at their N- or C-terminus (Fig. 13B).

Importantly, the presence of these transgenes restored flight ability and normal flight muscle organization, including sarcomere size (Fig. 13C and D) in the *fliI*-deficient flies, clearly demonstrating that addition of the FLAG tags does not disrupt the function of the FliI protein, and as such, it should be suitable for protein localization studies.

In sagittal sections of adult thoraces (~24 hours AE), we found that FliI is exclusively localized to the Z-discs of DLM myofibrils (independent of tag position) (Fig. 14). Additionally, we confirmed that FliI is localized to the Z-discs in individual myofibrils isolated from adult flies (~24 hours AE) or pupae (~72 hours APF, not shown here) as well, indicating a stable association with myofibrils both in developing and mature sarcomeres. To examine the distribution of FliI with higher resolution, we applied dSTORM nanoscopy combined with structure averaging (Szikora et al., 2020a). We found that FliI exhibits a distinctive "double-line" pattern along the Z-line, whether localized through the N or C-terminal FLAG tag, in both adult flies (~24 hours AE) (Fig. 14). The average Z-line peak distance was 53.43 nm for the N-terminal FLAG and 47.59 nm for the C-terminal FLAG tag in mature IFM (~24 hours AE). These positions (particularly the one of the N-terminus) are very similar to the position of CapZ, marking the edges of the Z-disc, and thereby the (+) end of the thin filaments (Pinter et al., 2020; Szikora et al., 2020a). These observations are entirely consistent with our previous *in vitro* results demonstrating a barbed end binding activity for the GH1-3 domains of *Drosophila* FliI (Pinter et al., 2020), and suggest that FliI may act as a barbed end binding protein at the Z-disc.

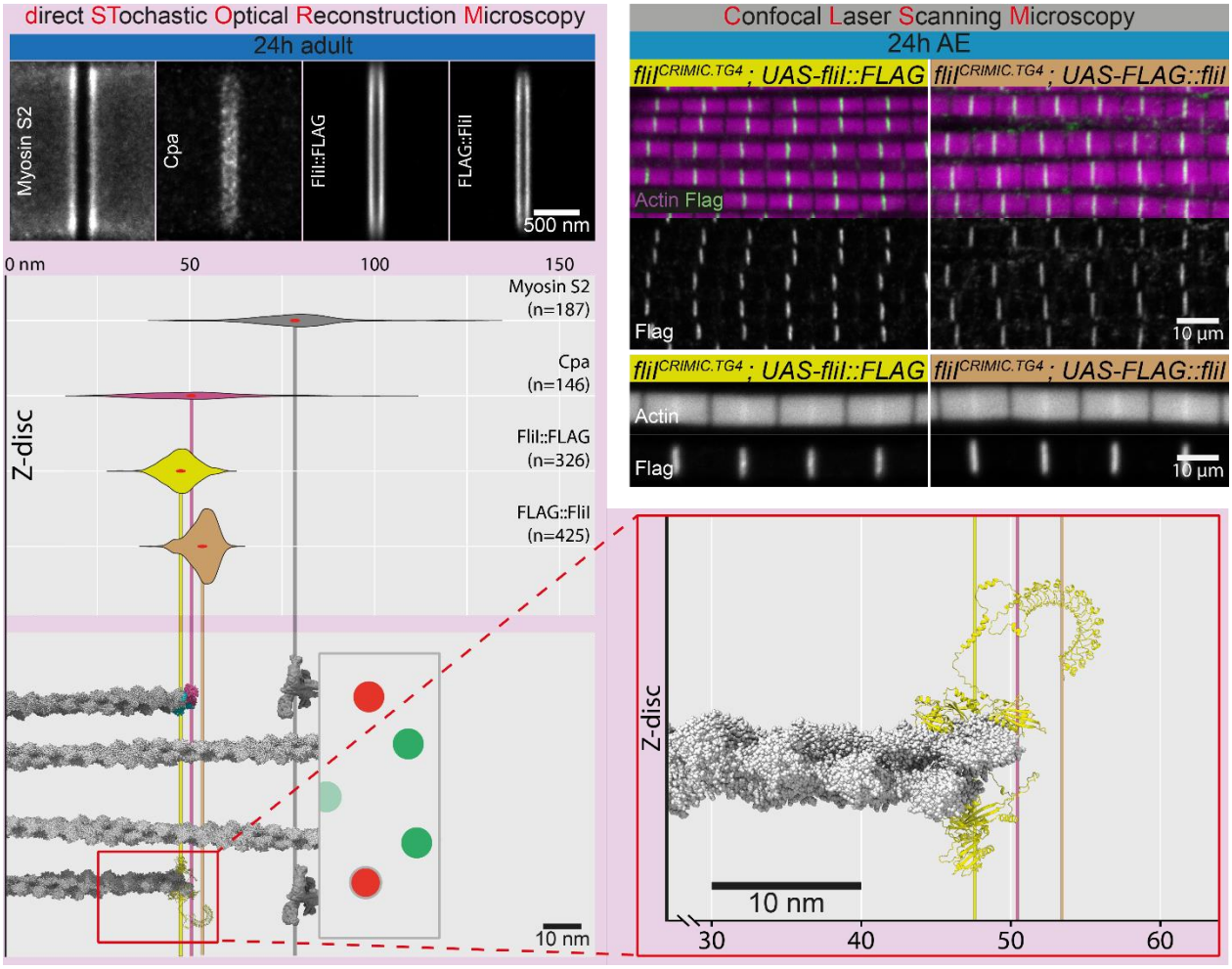

Figure 14. FliI localize at the Z-disc of sarcomeres at the barbed end. Top right: FliI localization in both whole muscle preparations and isolated myofibrils. Top left: Averaged dSTORM reconstructions display the localization of C- and N-terminally Flag-tagged FliI, alongside Myosin S2 and Cpa, which serve as reference markers for the Z-disc and the I-line edges, respectively. Bottom right: Scaled schematic representation of the Z-disc edge region, illustrating FliI binding at the barbed ends of actin filaments. The FliI structural model was generated using AlphaFold. Visualization was performed in ChimeraX, incorporating the 7pdz PDB structure as well as the EMD-3301 and EMD-8727 density maps.

FliI interacts with dLLRFIP2 in the flight muscle of *Drosophila*

Our results indicated that the FliI protein is involved in sarcomere development, but its molecular function or regulation still remained largely ambiguous, therefore, we sought to identify the potential molecular interaction partners of *fliI* specific to IFM. To this end, we employed affinity purification coupled with mass spectrometry, using the FLAG-tagged full length FliI constructs in rescue conditions in a protein-null background ($fliI^{CRIMIC.TG4}$). This approach enabled the isolation of the FliI associated proteins from thoracic lysates of mature (24h AE) and developing flies (72h APF, not shown here). Bioinformatic analysis of the mass-spec data led to the

identification of a single strong hit, corresponding to *CG8578* (Fig. 15), at both developmental stages, also corroborating previous findings in S2R+ cells (Guruharsha et al., 2011; Rhee et al., 2014). Moreover, we found that the mammalian orthologs of CG8578 were designated as LRR binding FliI interacting protein 1/2 (LRRFIP1/2) because of their ability to interact with FliI. Sequence analysis shows that the 396 amino acid long CG8578 protein contains a conserved 87-amino acid region corresponding to the FliI interaction surface identified in both LRRFIP1 and LRRFIP2. This region, critical for binding to FliI (Fong and de Couet, 1999), is present in all LRRFIP homologs, including *Drosophila* CG8578. Overall, CG8578 shares greater similarity with LRRFIP2 than LRRFIP1, as it has the best score in DIOPT v9.1 ortholog finder and also matches LRRFIP2 isoform 2 (401 amino acids long) in amino acid length, whereas LRRFIP1 is considerably longer. We therefore consider CG8578 as the *Drosophila* homolog of LRRFIP2. Despite the moderate level of sequence similarity between dLRRFIP2 and its human counterpart (43,1% identity and 62,2% positivity), the AlphaFold2 predictions reveal a high degree of 3D structural conservation, supporting the possibility that they share common *in vivo* binding partners.

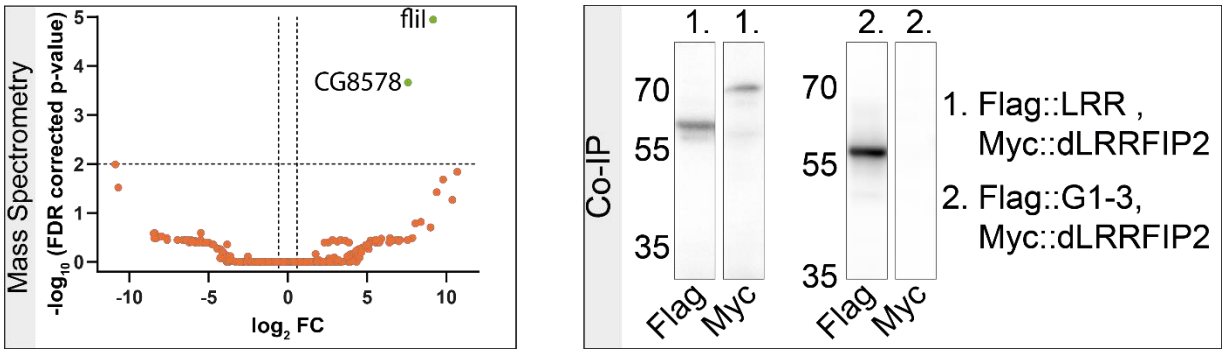

Figure 15. Identification of FliI interacting partners through immunaffinity purification and co-immunoprecipitation. Volcano plot shows proteins enriched (green) by FliI-Flag immunaffinity purification from IFM tissue, identified by mass spectrometry. The right panel shows the co-immunoprecipitation (co-IP) assay demonstrating that the LRR region of FliI is sufficient to pull-down Myc-tagged dLRRFIP2, supporting a direct or complex-mediated interaction.

To confirm results of the IP-MS analysis by independent means, we carried out a co-immunoprecipitation interaction assay with S2 cells transfected with FLAG::FliI-LRR and Myc::dLRRFIP2 expressing plasmids. These assays clearly confirmed that, unlike the GH regions of FliI, the FliI LRR region is able to pull-down dLRRFIP2 (Fig. 15, Supplementary Fig 1).

The knockdown of *dLRRFIP2* results in nearly identical muscle phenotypes as the lack of FliI

Given that dLRRFIP2 was identified as a potential FliI-binding protein, we wondered whether it plays a role in muscle development. To address this question, we examined the effect of muscle-specific knockdown of *dLRRFIP2* with two independent RNAi lines (VDRC KK and GD), and we found that the KD results in the loss of the flight ability and impairs myofibril organization (Fig. 16). Interestingly, we observed a reduction in sarcomere length and width, which was very similar to the effect of *fliI* KD (24 hours AE) (*dLRRFIP2KK* length:2.453±0.313µm, width:0.718±0.086µm; *dLRRFIP2GD* length: 2.595±0.288µm, width:0.913±0.081µm; FliI KD: length:2.451±0.316µm, width:0.714±0.09µm) (Fig. 16).

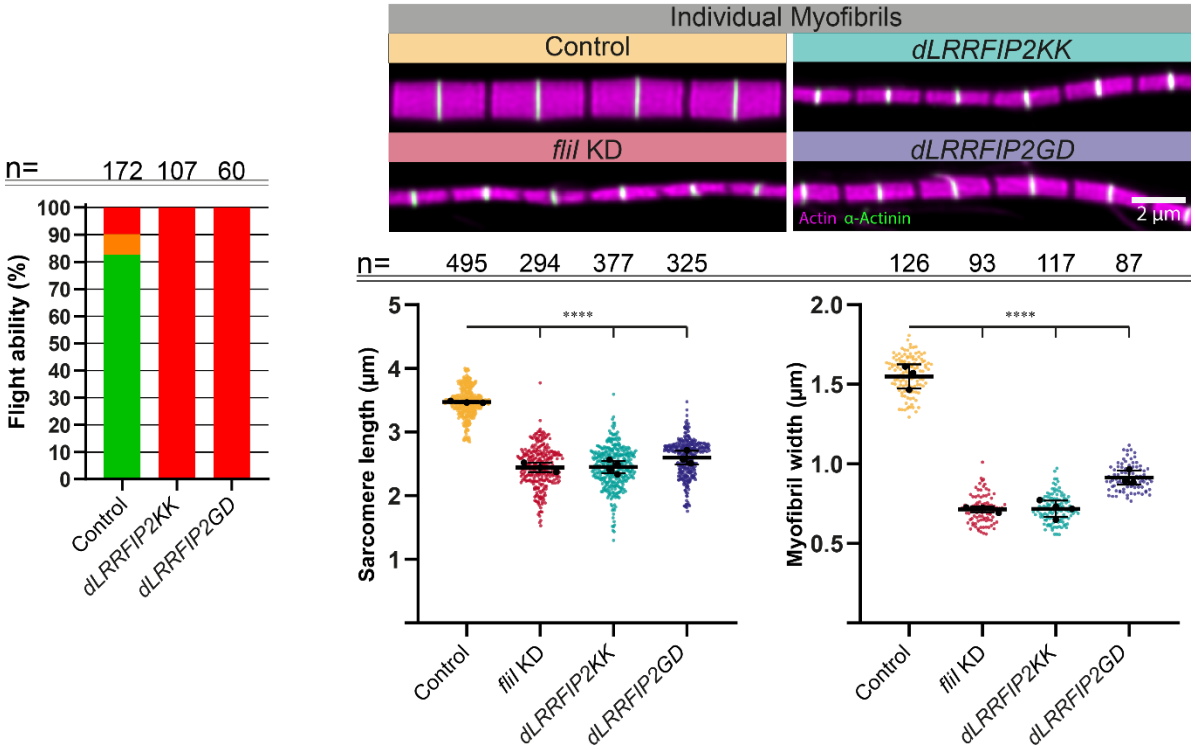

Figure 16. dLRRFIP2 knockdown mimics the effects of FliI depletion in IFM sarcomeres. The graph on the left shows the quantification of the flight ability in control and two different *dLRRFIP2* RNAi lines at 24h AE. "n" indicates the number of flies tested. On the right micrographs show the average myofilament structure in control, *fliI* and *dLRRFIP2* knockdown flies at 24h AE, stained with phalloidin and α-actinin to visualize the actin and Z-disc, respectively. The bottom right graphs show the quantification of sarcomere length and width in the same genotypes at 24h AE. Colored dots represent individual measurements of sarcomere length and myofibril diameter, while the larger black dots indicate the mean values from independent experiments. Error bars represent the mean and s.d. of independent experiments. "n" refers to the number of sarcomeres measured. Statistical analysis was performed using one-way ANOVA with Tukey's multiple comparison test

To extend these studies, a developmental analysis has also been carried out. Upon the KD of *dLRRFIP2* at 48 hours APF the sarcomeres were indistinguishable from the wild type (control

length: 2.164±0.224 µm, width: 0.363±0.051µm; *dLRRFIP2KK* length: 2.029±0.298µm, width: 0.472±0.096µm), but by 72 APF significant differences were observed both in length and width (control length: 2.834+0.227µm, width: 0.799±0.061µm; *dLRRFIP2KK* length: 2.297±0.181µm, width: 0.551±0.058µm), and these changes became even more obvious during the later stages of muscle development (Fig. 17A, B).

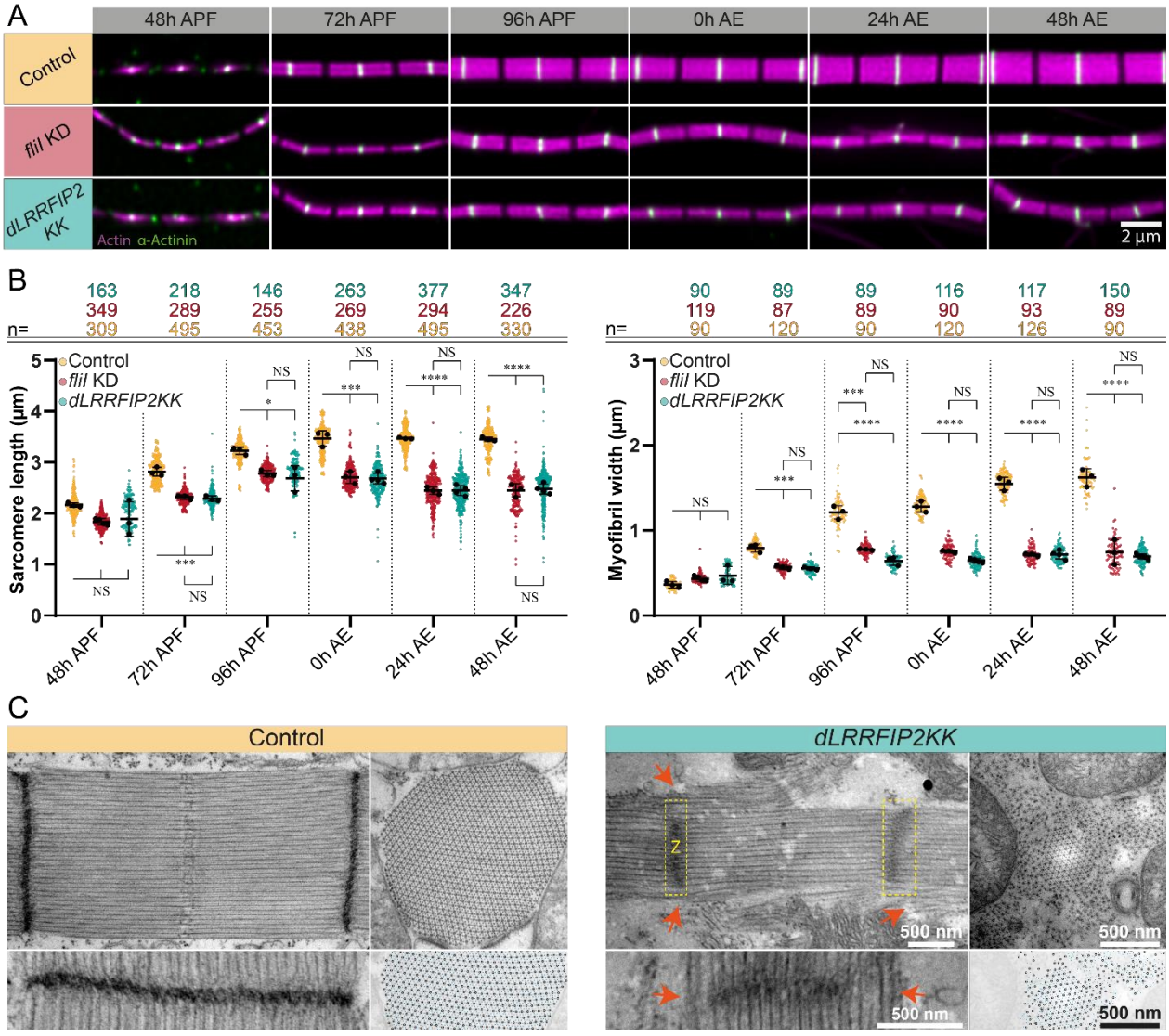

Figure 17. dLRRFIP2 is required during the steady growth phase of myofibrillogenesis. (A) Isolated Individual myofibrils represent the mean size of the sarcomeres at every measured time point. (B) Quantification of sarcomere length and width in control, *fliI* and *dLRRFIP2* knockdown flies at 6 different time points during the myofibrillogenesis. Colored dots represent individual measurements of sarcomere length and myofibril diameter, while the larger black dots indicate the mean values from independent experiments. Error bars represent the mean and s.d. of independent experiments. "n" refers to the number of sarcomeres measured**.** Statistical analysis was performed using one-way ANOVA with Tukey's multiple comparison test. (C) Electron micrographs of longitudinal sections from DLM fibers of control and *dLRRFIP2* knockdown flies at 24h AE. Red arrows indicate loosely connected or unintegrated filaments.

With TEM analysis of the *dLRRFIP2* KD muscles, we revealed the presence of impaired/smaller Z-discs and a high number of loosely connected peripheral filaments (Fig. 17C), much as in the case of *fliI* KD, together with the zebra body-like electron-dense structures and other actin aggregates (not shown here). Collectively, these striking phenotypic similarities strongly suggest that FliI and dLRRFIP2 work together during *Drosophila* IFM development.

The function of FliI is dependent on the presence of dLRRFIP2

To collect genetic evidence for the interaction of FliI and dLRRFIP2, an epistasis analysis was performed with the L674V mutant form of FliI, carrying a point mutation in the second GH domain and causing cardiomyopathy in human (Ruijmbeek et al., 2023). The overexpression of this form induces the formation of much wider myofibrils than normal, and a mild reduction of sarcomere length (Fig. 18). This observation further proves the involvement in radial growth regulation, and we used this overexpression background to knockdown the dLRRFIP2 protein. Remarkably, the absence of dLRRFIP2 completely suppressed the sarcomeric defects caused by the overexpression of FliI^{L674V} (Fig. 18), indicating that the function of FliI in radial sarcomere growth strictly depends on the presence of dLRRFIP2.

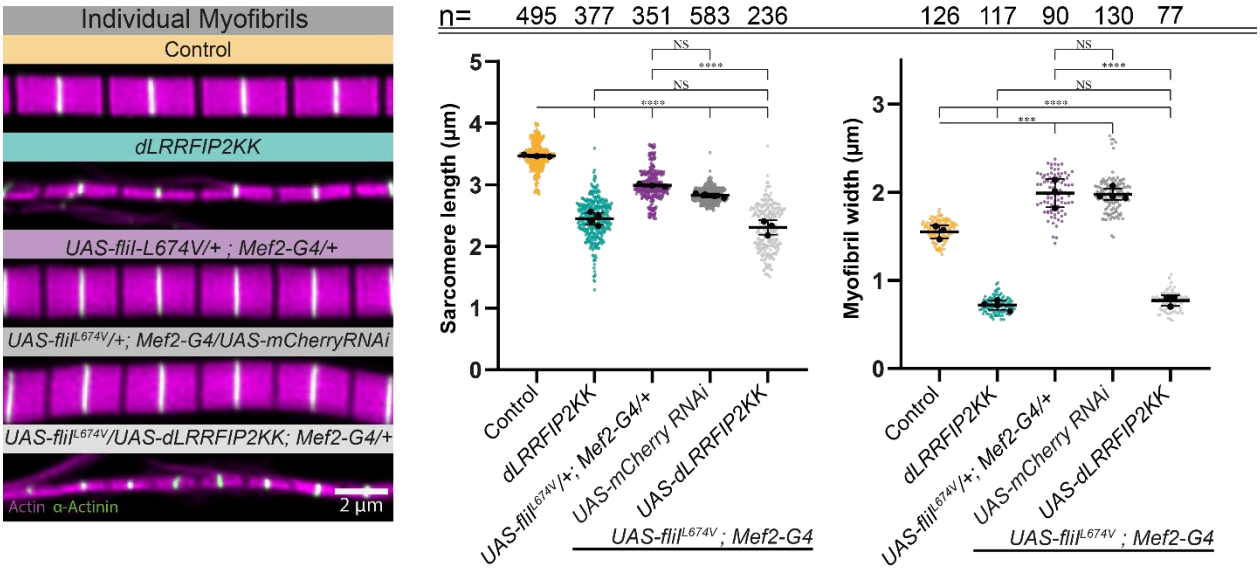

Figure 18. Genetic epistatic assay highlights that the *in vivo* function of FliI depends on the dLRRFIP2 presence. Isolated Individual myofibrils represent the mean size of the sarcomeres for every genotype 24h AE. The graph represents the quantification of sarcomere length and width in different genotype backgrounds. Colored dots represent individual measurements of sarcomere length and myofibril diameter, while the larger black dots indicate the mean values from independent experiments. Error bars represent the mean and s.d. of independent experiments. "n" refers to the number of sarcomeres measured. Statistical analysis was performed using one-way ANOVA with Tukey's multiple comparison test.

Molecular modelling of the FliI/dLRRFIP2 interaction

To gain insights into the molecular basis of the FliI/dLRRFIP2 interaction and its potential biological function, we used AlphaPulldown, a modelling pipeline based on AlphaFold2, developed by the Kosinski Lab (Molodenskiy et al., 2025; Yu et al., 2023). This approach enabled systematic modelling using different domains or domain combinations of FliI as "bait" and dLRRFIP2 as the "candidate" protein (Fig. 19A). Through this strategy, we aimed to predict both the molecular structure and the potential interaction interface of the FliI/dLRRFIP2 complex with high confidence.

In total, 100 domain to domain combinations were modelled, with five structural models generated per pair (Fig. 19B). Among these, 10 domain pairs achieved greater than 0.5 predicted template modelling (pTM) score and interface pTM (ipTM) score at the same time, which is generally considered a meaningful cutoff for potentially relevant interactions worth looking into further. After a detailed assessment of the pLDDT confidence scores of these models, six unique domain combinations were selected for further interpretation. Notably, all six selected models consistently featured the LRR region of FliI and Helix2 of dLRRFIP2, suggesting that, similarly to humans, in *Drosophila* the interaction is facilitated by these two regions (Fig. 19B). Structural comparison of these models revealed that AlphaFold2 predicted two distinct interaction interfaces on the LRR domain, referred to as Binding Site 1 (BS1) and Binding Site 2 (BS2) (Fig. 19B). Of the 30 high confidence models derived from the six selected combinations, 16 were aligned with BS1 and 14 with BS2. Importantly, based on modeling, these two binding modes do not appear to be mutually exclusive. Structural inspection indicates that both interfaces could be occupied simultaneously, implying that Helix2 of dLRRFIP2 likely dimerizes to interact with the FliI LRR region (Fig. 19B). This hypothesis is supported by prior reports on the human ortholog LRRFIP1, which is known to form dimers via its coiled-coil region, which is structurally analogous to Helix2 of dLRRFIP2 (Nguyen and Modis, 2013). Consistently, AlphaFold2 was able to model the dimeric structure of this region. To support this prediction, we also performed biochemical assays, which confirmed that dLRRFIP2 can indeed form dimers under physiological conditions, reinforcing the idea that the dimerization of Helix2 plays a key role in mediating the interaction with FliI (Fig. 19C).

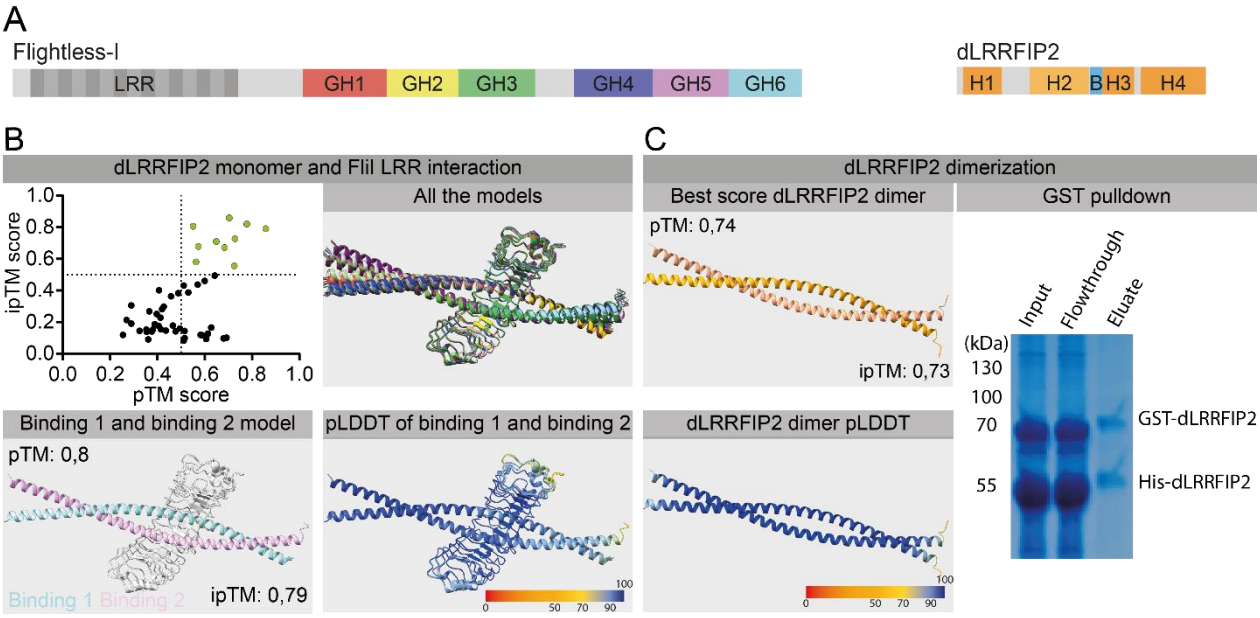

Figure 19. Structural modeling of FliI LRR region interaction with dLRRFIP2, and the dLRRFIP2 dimerization using AlphaPulldown. (A) Scaled schematic representation of FliI and dLRRFIP2, highlighting their domain compositions. (B) Scatter plot illustrating the correlation between pTM and ipTM for all AlphaFold-generated interaction models of FliI and dLRRFIP2 in various domain combinations. Dotted lines mark the 0.5 threshold for both metrics; green dots indicate high-confidence models exceeding this threshold. Imagies showing the Superposition of all high-scoring models and binding 1 and binding 2 of dLRRFIP2 with or without AlphaFold's per-residue confidence score (pLDDT) coloring, aligned via the LRR region of FliI. (C) Structural view of Helix2 from the top-scoring dimer model of dLRRFIP2. Coomassie-stained SDS-PAGE gel showing the results of a GST pulldown assay using co-expressed GST-tagged and His-tagged dLRRFIP2 in *E. coli* cells.

To further validate this model, we extended the analysis by modelling a trimeric complex involving the FliI LRR domain and a dimerized form of dLRRFIP2. Out of 20 possible trimeric configurations, 9 models had sufficiently high confidence scores (Fig. 20A). Across these nine combinations, all 90 models consistently featured dimerization of dLRRFIP2 through Helix2, with the resulting interface engaging the inner surface of the FliI LRR domain. When comparing this interaction to the individual binding sites (BS1 and BS2), the dimer-based interaction was nearly identical, with only minor differences observed at the C-terminus of Helix2. The interaction surface on the LRR domain remained consistent across models. To identify the important residues in this interaction we used chimera contact finding algorithms combined with PDBePISA, a tool created to explore macromolecular interfaces (Fig. 20B). The combination of these two tools allowed us to identify 10 highly conserved residues in dLRRFIP2 which is important, as changing 8 of these 10 residues results in the complete disruption of the interaction, at least in our *in silico* models.

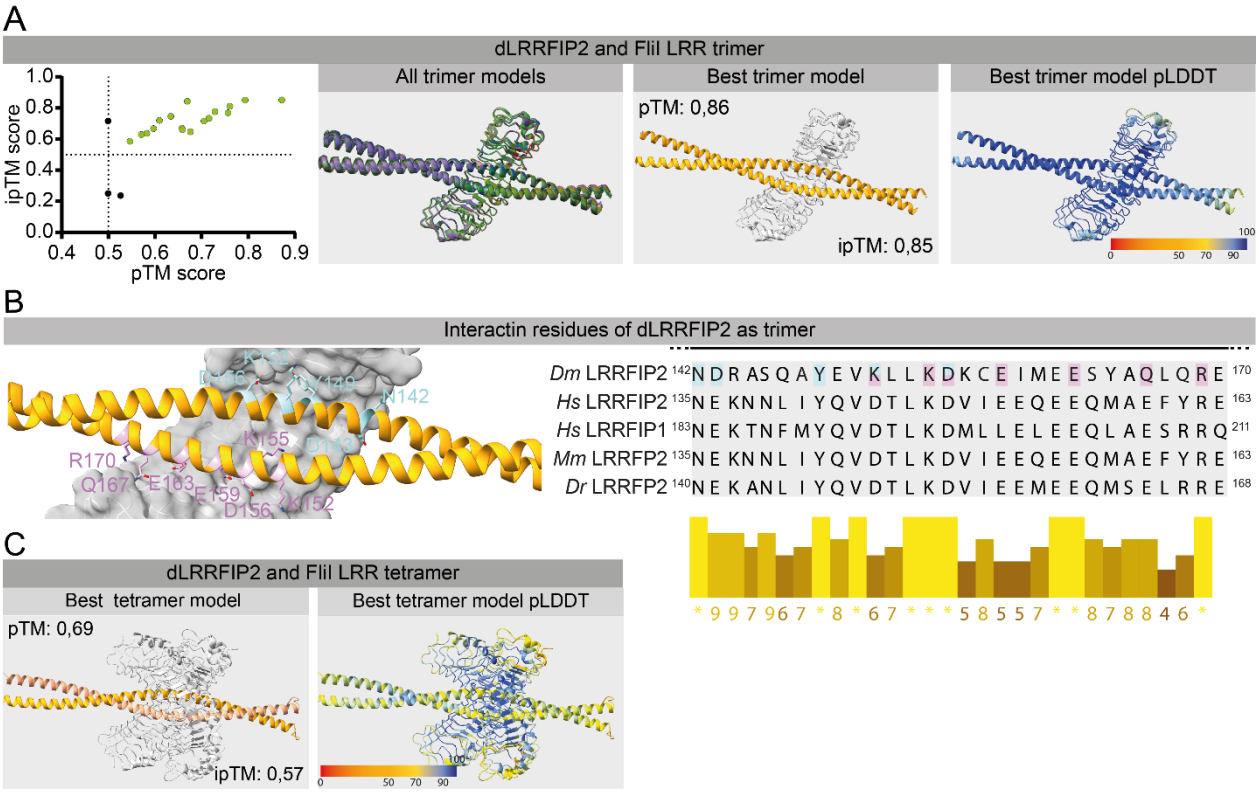

Figure 20. The LRR region is able to interact with a dLRRFIP2 dimer. (A) Scatter plot showing the correlation between predicted pTM and ipTM for all AlphaFold-generated models of FliI and dLRRFIP2 trimerization. Dotted lines indicate the 0.5 threshold for each score. All models are shown aligned via the LRR domain of FliI. The best-scoring structural model highlights a dLRRFIP2 dimer (orange helix) interacting with the LRR domain of Flightless-I, displayed with and without per-residue confidence coloring (pLDDT). (B) Zoomed-in view of the interface between dLRRFIP2 and the LRR domain of Flightless-I, showing key interacting residues. A sequence alignment of dLRRFIP2 with LRRFIP2 orthologs from Homo sapiens, Mus musculus, and Danio rerio is included, emphasizing conserved regions across species. (C) The image shows the best scored tetramer model for LRR and dLRRFIP2 interaction.

These findings demonstrate that AlphaFold2 was not only able to identify two plausible binding interfaces on the LRR domain but also correctly modelled the interaction of both monomeric and dimeric dLRRFIP2 with FliI. The reproducibility and confidence of these models support a conserved, dimer-facilitated interaction mechanism between the two proteins. This likely reflects a biologically relevant arrangement that could potentially stabilize FliI's association with actin structures or coordinate its activity in sarcomere assembly. Although our data do not support a single, consistent structural model for a higher-order tetrameric complex, AlphaFold2 generated models of a potential 2:2 FliI-dLRRFIP2 tetrameric complex with moderate confidence scores (pTM score of 0.69 and an ipTM score of 0.57). While these values fall below of high-confidence thresholds, they suggest a non-negligible likelihood of tetramer formation under certain conditions.

The inconsistency observed across structural predictions may reflect underlying flexibility, transient binding behavior, or the necessity of additional stabilizing components such as actin filaments or regulatory cofactors. However, we note that if such a tetrameric configuration occurs *in vivo*, it could act as a platform for actin cross-linking or cytoskeletal coordination during myofibrillogenesis. Further experimental validation will be essential to determine the physiological relevance and functional significance of this possible higher-order assembly.

6. Discussion

Sarcomere size must be precisely regulated to ensure proper contraction efficiency, a key characteristic of each muscle. Mutations affecting the thin filament components could lead to structural alterations that are the molecular basis for several debilitating muscle diseases (de Winter and Ottenheijm, 2017; Parker et al., 2020). Therefore, understanding the mechanisms of thin filament development in detail would not only reveal a basic biological phenomenon but would also help to design novel strategies to combat devastating human skeletal and cardiac muscle diseases. An important step toward this goal is to identify all proteins contributing to the regulation of thin filaments. Beyond the missing players, we also lack answers for a number of mechanistic questions. These include the mechanisms of initial actin assembly, pointed end elongation, radial growth of the arrays via peripheral actin assembly, the coordination of thin and thick filament growth and a unifying theory about thin filament length regulation. To address some of these questions, we chose the *Drosophila* indirect flight muscle as our model system. In addition to the excellent genetic toolkit available in fruit flies, this model system offers the possibility to study sarcomere development with high spatial and temporal resolution. Since there is no comprehensive research thoroughly detailing sarcomere development from the actin side, to begin with, we used a multiscale morphometric approach to describe IFM growth during development in great detail by going down to the level of individual myofilaments.

To assess the changes in myofibril/sarcomere size we initially used confocal microscopy to visualize the structures at 12 different time points spanning from 36 hours APF to 96 hours AE. Despite other studies measuring sarcomere size in adults or during myofibrillogenesis, the reported values often vary significantly between laboratories (Chakravorty et al., 2017; Fernandes and Schock, 2014; Orfanos and Sparrow, 2013; Reedy and Beall, 1993; Shwartz et al., 2016; Spletter et al., 2018). Such differences are most likely caused by inconsistent sample preparation, varying

imaging resolution, and differences in measurement approaches. In our study, we highlighted how differences in sample type and preparation can significantly affect morphometric measurements (Görög et al 2025). Furthermore, the measurement methodology itself represents a critical source of variability that likely contributes to the inconsistencies reported across studies. Therefore, we sought to address these challenges and tried out several dedicated automated tools for sarcomere morphometric analysis (Baheux Blin et al., 2024; Neininger-Castro et al., 2023; Spletter et al., 2018; Zhao et al., 2021). However, none achieved the required level of accuracy and efficiency on our dataset, particularly in simultaneously measuring both parameters. Therefore, we developed a custom, Python-based segmentation and measurement algorithm tailored to the specific characteristics of our imaging data. To measure the length, after separating the channels, the software records the histogram profile along the myofibril on a channel containing Z-disc specific staining, and fits multiple Gaussian functions to determine the peak coordinates and therefore the peak distances, corresponding to the length of the sarcomeres. For myofibril width, the intensity profile is recorded perpendicular to the myofibril and a "disk function" is fitted to estimate the diameter. We tested this algorithm in our simulated sarcomere test data, and it was able to reliably determine both parameters. In our practice, the application of this software tool not only improves the accuracy of our measurements, but it also results in a very significant, roughly twenty-fold increase in analysis speed.

The first myofibril precursors, which already contain periodic sarcomere-like structures, appear at around 30 hours APF (Spletter et al., 2018; Weitkunat et al., 2014), however, these early myofibrils are still composed of largely disorganized myofilaments. As compared to this, our developmental analysis of sarcomere structure using confocal microscopy revealed that the earliest stable sarcomeres appear at 36 hours APF. TEM images have shown that these structures mostly lack the regular hexagonal lattice arrangement, but in the following 12 hours the organization becomes more ordered, with a nearly perfect hexagonal pattern and a 1:3 thick to thin filament ratio. During this period, the Z-disc and M-line specific proteins, such as Kettin, Sls700, Zasp52, α-actinin and Obscurin (Weitkunat et al., 2014) start to localize in a periodic manner, although we found that the Z-disc association of α-actinin and Zasp52 is not completely stable yet because it can be easily disrupted by detergents used during individual myofibril preparations (Görög et al 2025). Our measurements of the developing muscles also revealed that between 36-48 hours APF, sarcomere size remains largely unchanged, while the structure clearly becomes more regular.

Therefore, we refer this first part of the development as the “organization phase”. After their initial formation, sarcomeres start to grow significantly in a stable manner, therefore, we refer to this subsequent phase as the “steady growth phase”. Despite being shorter and thinner, during this phase the gross ultrastructure of the sarcomeres highly resembles to that of the adults. In regard of growth dynamics, we found a consistent rate up to 96 hours APF, after which we observed a sharp increase in sarcomere length until eclosion (0 hours AE), likely due to pre-stretching of the IFM myofibrils as the thoracic exoskeleton expands. Our data also showed that IFM sarcomere length and diameter generally peak and/or plateau in young adult flies around 12 hours AE. During the steady growth phase, not only the already existing filaments grow, but new myofilaments form as well and integrate into the already existing sarcomeric structure, thereby contributing to radial growth of the sarcomeres. The mechanisms driving the coordinated elongation and thickening of the sarcomeres remained largely unclear. Although several proteins involved in filament lengthening have been identified, elongation from the pointed end is still a mysterious process (Farkas et al., 2024; Littlefield and Fowler, 2008; Molnar et al., 2014; Spletter et al., 2018). Similarly, the mechanisms underlying radial growth and the main molecular players involved in this process are still largely unknown. During my work, I identified two potential new factors involved in peripheral sarcomere growth, and we expected that their functional characterization will shed light on this important process.

While previous studies have provided some insights into the muscle-specific function of FliI, a comprehensive molecular model explaining its mode of action is still lacking (Campbell et al., 1993; Deng et al., 2021; Kuwabara et al., 2023; Miklos and De Couet, 1990; Perrimon et al., 1989; Ruijmbeek et al., 2023; Schnorrer et al., 2010). We used a complex approach to uncover the molecular mechanism by which the conserved FliI protein regulates myofibrillar structure and growth. Earlier studies revealed that the depletion of FliI leads to an abnormal flight muscle morphology and flightlessness (Campbell et al., 1993; Deng et al., 2021; Miklos and De Couet, 1990; Perrimon et al., 1989; Schnorrer et al., 2010). Our loss of function analysis with two hypomorphic alleles and an RNAi line further confirms these observations. The hypomorphic alleles and the knockdown of the protein results in complete flightlessness coupled with abnormal IFM morphology. Loss of the FliI function causes the formation of F-actin rich protein aggregates both on the surface and among of the DLM fibers. Additionally, our results revealed that the flight muscle fibers are present in the expected numbers and can achieve close to normal size in *fliI*

deficient animals. Importantly, higher resolution images of these myofibrils unveiled a significant reduction in their width and shortened sarcomere length as compared to the wild type.

Our ultrastructural analysis of *fliI* KD DLM fibers revealed that the peripheral regions of the sarcomeres are particularly affected by the absence of FliI. TEM sections (including longitudinal and cross-sections) showed that the Z-disc is primarily confined to the central region of the myofibrils. Parallel to that, the surrounding peripheral filaments (thin and thick filaments as well) appeared loosely connected or entirely detached from the Z-disc, while the core region of the myofibrils exhibited a largely intact sarcomere organization, with a regular hexagonal lattice, normal thin to thick filament ratio, and a proper thick filament spacing. This suggests that the early steps of sarcomere organization proceed relatively normally in the absence of FliI, implying that FliI is not essential during the "organization phase" of sarcomere formation when proto-sarcomeres assemble, but it becomes critical in the subsequent "steady growth phase," where sarcomeres expand laterally and new filaments must be stably incorporated into the lattice. In addition to these defects, we also observed zebra body-like structures, which are typically associated with disrupted actin dynamics and are often found in muscle pathologies (Kuwabara et al., 2023; Lake and Wilson, 1975). These abnormalities, together with the accumulation of unanchored thin filaments in the adjacent cytoplasm, resulted in prominent actin-rich aggregates between neighboring myofibrils, which were clearly visible by confocal imaging. A similar phenotype was reported by Deng et al. in *fliI* KD muscles, where they interpreted the formation of these actin bundles as a consequence of reduced filament severing activity in the absence of FliI, leading to uncontrolled actin polymerization. Their model was based on FliI's localization at the Z-disc and the actin bundles that appeared to originate from this region. However, recent in-depth *in vitro* analyses concluded that FliI does not possess actin-severing activity, casting doubt on this interpretation (Mohammad et al., 2012; Pinter et al., 2020). Our findings suggest an alternative explanation. Rather than affecting actin polymerization directly, FliI appears to be essential for the proper incorporation and stabilization of thin filaments into the expanding sarcomeric lattice during myofibril growth. In the absence of FliI, filament integration is compromised, leading to excess actin filaments that fail to become stably anchored. Some of these filaments may remain loosely associated with the Z-disc, creating the appearance that actin bundles emerge directly from the Z-disc, visible by confocal microscopy. Therefore, we propose that FliI plays a key role in sarcomere organization without

having a major contribution to actin filament formation, rather by being required for their spatial coordination and incorporation during lateral myofibril expansion.

The localization of a protein provides critical insights into its function and role in the cellular processes. As to *Drosophila* FliI, former work, using a heterologous antibody raised against the human protein, led to conflicting results regarding the myofibrillar localization. Schnorrer et al. 2010 reported that the protein is present at the Z-disc and in the H-zone, whereas Deng et al. 2021 described a purely Z-disc accumulation. To address these discrepancies and to determine the localization of FliI in the IFM by independent means, we employed a genetic approach where the FLAG-tagged version of FliI was expressed in a *fliI* protein-null background ($fliI^{CRIMIC.TG4}$). These studies revealed a Z-disc enrichment in the mature and in the growing muscles as well, both with the N- and C-terminally tagged isoforms. Super-resolution analysis allowed us to refine the position of the protein to the edges of the Z-disc, near the (+) end of the actin filaments, which is in good accordance with former *in vitro* data revealing a (+) end binding ability for the GH1-3 domains of FliI (Pinter et al., 2020). Thus, the strong Z-disc accumulation provided further support for a role in Z-disc formation and peripheral myofilament integration, already suggested by the phenotypic data.

Although the investigation of FliI already resulted in numerous novel discoveries with potentially interesting functional implications, to better understand its molecular function, we thought to identify its IFM specific interaction partners, using affinity purification coupled with mass spectrometry. This approach led to the identification of a single strong candidate, corresponding to dLRRFIP2. The interaction was confirmed by Co-IP experiments, also revealing that the interaction is mediated by the LRR region of FliI and an 87 amino acid long conserved region of dLRRFIP2. If it was a functionally important interaction, we expected that dLRRFIP2 is required for muscle development, and indeed, we found that the knockdown of dLRRFIP2 not only impairs IFM development, but it results in nearly identical phenotypic effects as the silencing of *fliI*. In the absence of dLRRFIP2 the sarcomeres are shorter and thinner than in wild type, and the TEM images display smaller Z-discs and a large number of unintegrated myofilaments at the periphery of the myofibrils. Beyond the highly similar phenotypes, the cooperation between the two proteins is supported further by our genetic epistasis tests as well, when the silencing of dLRRFIP2 completely suppressed the gain-of-function effect caused by overexpression of the L674V point mutant form of FliI. Collectively, these results established that FliI and dLRRFIP2

work together during muscle development, and acting as Z-disc proteins, they have a critical contribution to peripheral myofibril growth.

To understand the molecular basis of the interaction between FliI and dLRRFIP2, we employed AI-based structural modeling. These studies revealed that, similar to its vertebrate ortholog LRRFIP1, dLRRFIP2 is highly likely to be able to form homodimers. In addition, this approach allowed us to model the FliI-dLRRFIP2 interaction as well, and to predict the interaction surfaces on the FliI LRR domain that can bind the dimerized Helix 2 of dLRRFIP2. In support of this, our biochemical assays also confirmed that the purified dLRRFIP2 protein is able to dimerize. Furthermore, analysis of the residues involved in the presumed interaction between FliI and dLRRFIP2 indicated that these are highly conserved residues, suggesting that they might contribute to an evolutionary conserved mechanism.

Taken together, our findings strongly suggest that FliI and dLRRFIP2 function as critical regulators of peripheral sarcomere growth, possibly through a cooperative action at the Z-disc, facilitating myofilament incorporation during growth. Based on our structural analyses, we hypothesize that these two proteins may form a heterotetrameric complex that acts as a specialized actin crosslinker. Such a complex could provide the structural basis for the stable incorporation and anchoring of newly formed actin filaments into the growing sarcomeric lattice, thereby facilitating lateral expansion of the myofibrils. This model would offer a plausible explanation for the unanchored peripheral filaments and actin aggregates observed in the absence of FliI or dLRRFIP2. In addition to this structural role, previous studies have proposed that FliI may act as a formin activator, influencing actin polymerization through interactions with Diaphanous-related formins (Deng et al., 2021; Higashi et al., 2010). Although we did not directly assess this activity in our study, our preliminary epistasis assays suggest a genetic interaction between FliI and the formins DAAM and Fhos (Dávid Farkas, unpublished results). This, combined with our observation that sarcomeres are not only thinner but also significantly shorter in FliI-deficient muscles, raises the intriguing possibility that FliI contributes to filament elongation as well. Thus, FliI may function at multiple levels of sarcomere assembly, promoting both the growth and proper incorporation of actin filaments, most likely through its coordinated action at the Z-disc. Finally, the functional importance of FliI in muscle physiology is further emphasized by recent human studies linking mutations in *fliI* to cardiomyopathy (Kuwabara et al., 2023; Ruijmbeek et al., 2023). These findings support a conserved role for FliI in sarcomere formation and maintenance across

species and highlight the potential clinical relevance of uncovering its precise molecular function. Further studies will be needed to determine whether the FliI-dLRRFIP2 complexes indeed possess actin crosslinking or nucleation-regulating activity, and to explore whether modulating their function could offer new therapeutic avenues in muscle diseases.

7. Summary

Precise control of sarcomere size is critical for muscle function, and perturbations in thin filament organization are a hallmark of many skeletal and cardiac myopathies. While sarcomere growth appears deceptively regular, the underlying mechanisms—especially those controlling radial expansion and pointed-end elongation—remain poorly understood. Using the genetically tractable *Drosophila* indirect flight muscle (IFM), we investigated the developmental dynamics of sarcomere size regulation with high spatial and temporal resolution.

We developed a custom Python-based analysis pipeline enabling rapid quantification of sarcomere length and width from fluorescence microscopy images. By applying this tool to wild-type IFM samples spanning 12 time points (36 h after puparium formation to adulthood), we defined two distinct growth phases. An initial "organization phase" (36–48 h APF) is characterized by sarcomere pattern refinement without size increase. This transitions into a prolonged "steady growth phase," marked by coordinated elongation and lateral expansion.

To identify molecular players in sarcomere size control, we focused on the conserved actin regulator Flightless I (FliI). FliI mutants displayed flightlessness, myofibrillar disarray, and sarcomeres that were significantly shorter and thinner than wild type. Transmission electron microscopy revealed selective defects at the sarcomere periphery, where thin filaments failed to properly integrate despite normal central architecture. These findings suggest FliI is required specifically for lateral filament addition during radial growth.

We next identified dLRRFIP2 as a robust interactor of FliI. Muscle-specific knockdown of dLRRFIP2 recapitulated key aspects of the FliI phenotype. Both proteins colocalized at the Z-disc region, near actin filament barbed ends. Co-immunoprecipitation and structural modeling revealed a direct interaction between the FliI leucine-rich repeat (LRR) domain and a conserved region of dLRRFIP2. We propose that this interaction facilitates the formation of an actin-crosslinking complex at the sarcomere periphery.

Altogether, our results identify FliI and dLRRFIP2 as essential components of peripheral sarcomere expansion. We propose a model in which they stabilize newly formed actin filaments at the Z-disc, ensuring correct integration into the growing myofibril. Given emerging links between human FliI variants and cardiomyopathy, this mechanism may be evolutionarily conserved and clinically relevant for understanding muscle pathologies.

8. Funding

Hungarian Scientific Research Fund (OTKA) (K132782 to József Mihály); Hungarian Scientific Research Fund (OTKA) (FK138894 to Szilárd Szikora); ÚNKP-22-3-SZTE-252 and ÚNKP-23-3; SZTE-315 New National Excellence Program of the Ministry for Innovation and Technology from the source of the National Research, Development and Innovation Fund (to Péter Görög and Szilárd Szikora)

9. Acknowledgment

I would like to express my deepest appreciation to my supervisor, **Dr. József Mihály**, for providing an inspiring research environment and for his unwavering support. His thoughtful advice, constructive discussions, and high standards have shaped this thesis and have consistently challenged me to grow as a scientist. His leadership and commitment to scientific excellence have been a continual source of motivation and have taught me the importance of curiosity, integrity, and perseverance in research.

I am sincerely grateful to **Dr. Szilárd Szikora** for his invaluable guidance, constant support, and encouragement throughout my doctoral research. His expertise, insightful feedback, and patience have been fundamental both to my development and to the completion of this work. His attention to detail and willingness to share his knowledge have greatly deepened my understanding of the field and have inspired me to approach scientific problems with critical thinking and creativity.

I would also like to thank **Dr. Ferenc Jankovics** and **Dr. István Földi** for their guidance during the early stage of my studies. They taught me the basics of laboratory work, and I have relied on this knowledge and their expertise throughout my research. I am grateful all the current and previous members of the Laboratory of Actin Cytoskeleton Regulation: **Dr. Krisztina Tóth**, **Alexandra Tóth**, **Dr. Balázs Vedelek**, **Dr. Rita Gombos**, **Dr. Dávid Farkas**, **Dr Gabriella Gazsó-Gerhát**, **Dr. Péter Kaltenecker**.

I am also grateful to all the members of the Department of Genetics for their help and support.

Last but not least, it is difficult for me to express the depth of gratitude I owe to my family. Their unwavering support, understanding, and encouragement have sustained me throughout this journey. Without their help, patience, and belief in me, this work would not have been possible.

10. Supplementary

Software	Licence	Programming knowledge required	Data Input	Accurate sarcomere length measurement	Accurate myofibril width measurement
IMA	Open source	Not required	Compatible with raw microscope image formats	Yes	Yes
MyofibrilJ	Open source	Not required	Requires preprocessing	Significantly underestimates	Significantly underestimates
SarcGraph	Open source	Intermediate (Python; requires manual parameter setup)	Requires preprocessing	Yes	Significantly underestimates
sarcApp	Commercial (PySimpleGUI 5)	Intermediate (Python; requires manual parameter setup)	Requires preprocessing	Yes	Yes

Supplementary Table 1. Comparison of the major features of the software tools suitable for IFM sarcomere morphometric analysis. This table compares IMA with three other software tools available for analyzing individual IFM myofibril images labeled with both phalloidin and Z-disc markers. Among these, IMA demonstrated the highest efficiency and/or accuracy for this specific task.

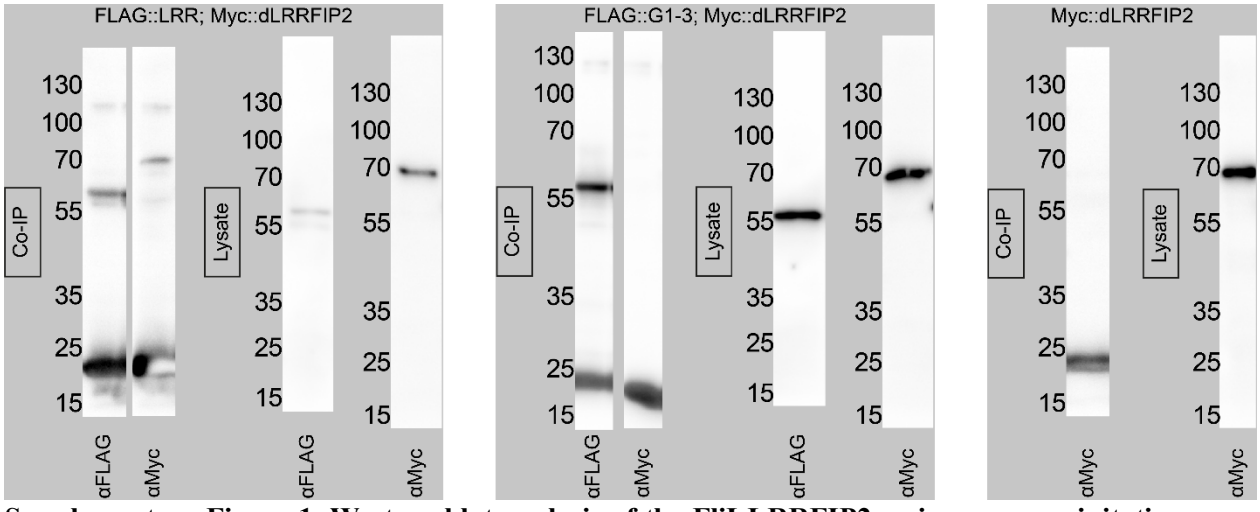

Supplementary Figure 1. Western blot analysis of the FliI-LRRFIP2 co-immunoprecipitation assay carried out with S2 cell lysates. The left panel shows the complete blot for the Co-IP and total lysate from cells co-expressing FLAG::LRR and Myc::dLRRFIP2. The middle panel shows the complete blot for the Co-IP and total lysate from cells co-expressing FLAG::G1-3 and Myc::dLRRFIP2. The right panel shows the complete blot for the Co-IP and total lysate from cells expressing Myc::dLRRFIP2.

Co-author certification

I, myself as a corresponding author of the following publication(s) declare that the authors have no conflict of interest, and Péter Görög Ph.D. candidate, had a significant contribution to the jointly published researches. The results discussed in his thesis were not used and not intended to be used in any other qualification process for obtaining a PhD degree.

2025.09.09

date

author

The publication(s) relevant to the applicant's thesis:

I. Szikora Szilárd; Görög Péter; Mihály József. The mechanisms of thin filament assembly and length regulation in muscles. INTERNATIONAL JOURNAL OF MOLECULAR SCIENCES 23 : 10 Paper: 5306 , 25 p. (2022)

II. Szikora Szilárd; Görög Péter; Kozma Csaba; Mihály József. *Drosophila* models rediscovered with super-resolution microscopy. CELLS 10 : 8 Paper: 1924 , 22 p. (2021)

11. References

Al-Hassnan, Z.N., A. Almesned, S. Tulbah, A. Alakhfash, F. Alhadeq, N. Alruwaili, M. Alkorashy, A. Alhashem, A. Alrashdan, E. Faqeih, S.M. Alkhalifi, Z. Al Humaidi, S. Sogaty, N. Azhari, A.M. Bakhaider, A. Al Asmari, A. Awaji, B. Albash, M. Alhabdan, M.A. Alghamdi, W. Alshuaibi, R.Z. Al-Hassnan, A. Alshenqiti, A. Alqahtani, Z. Shinwari, M. Rbabeh, S. Takroni, A. Alomrani, D.C. Albert Brotons, A.M. AlQwaee, W. Almanea, F.A. Alfadley, M. Alfayyadh, and A. Alwadai. 2020. Categorized Genetic Analysis in Childhood-Onset Cardiomyopathy. *Circ Genom Precis Med*. 13:504-514.

Amandio, A.R., P. Gaspar, J.L. Whited, and F. Janody. 2014. Subunits of the Drosophila actin-capping protein heterodimer regulate each other at multiple levels. *PLoS One*. 9:e96326.

Babcock, G., and P.A. Rubenstein. 1993. Control of profilin and actin expression in muscle and nonmuscle cells. *Cell Motil Cytoskeleton*. 24:179-188.

Baheux Blin, M., V. Loreau, F. Schnorrer, and P. Mangeol. 2024. PatternJ: an ImageJ toolset for the automated and quantitative analysis of regular spatial patterns found in sarcomeres, axons, somites, and more. *Biol Open*. 13.

Campbell, H.D., S. Fountain, I.S. McLennan, L.A. Berven, M.F. Crouch, D.A. Davy, J.A. Hooper, K. Waterford, K.S. Chen, J.R. Lupski, B. Ledermann, I.G. Young, and K.I. Matthaei. 2002. Fliih, a gelsolin-related cytoskeletal regulator essential for early mammalian embryonic development. *Mol Cell Biol*. 22:3518-3526.

Campbell, H.D., T. Schimansky, C. Claudianos, N. Ozsarac, A.B. Kasprzak, J.N. Cotsell, I.G. Young, H.G. de Couet, and G.L. Miklos. 1993. The Drosophila melanogaster flightless-I gene involved in gastrulation and muscle degeneration encodes gelsolin-like and leucine-rich repeat domains and is conserved in Caenorhabditis elegans and humans. *Proc Natl Acad Sci U S A*. 90:11386-11390.

Carlier, M.F., and D. Pantaloni. 1997. Control of actin dynamics in cell motility. *J Mol Biol*. 269:459-467.

Carroll, S., S. Lu, A.H. Herrera, and R. Horowits. 2004. N-RAP scaffolds I-Z-I assembly during myofibrillogenesis in cultured chick cardiomyocytes. *J Cell Sci*. 117:105-114.

Carroll, S.L., A.H. Herrera, and R. Horowits. 2001. Targeting and functional role of N-RAP, a nebulin-related LIM protein, during myofibril assembly in cultured chick cardiomyocytes. *J Cell Sci*. 114:4229-4238.

Chakravorty, S., B.C.W. Tanner, V.L. Foelber, H. Vu, M. Rosenthal, T. Ruiz, and J.O. Vigoreaux. 2017. Flightin maintains myofilament lattice organization required for optimal flight power and courtship song quality in Drosophila. *Proc Biol Sci*. 284.

Chesarone, M.A., A.G. DuPage, and B.L. Goode. 2010. Unleashing formins to remodel the actin and microtubule cytoskeletons. *Nat Rev Mol Cell Biol*. 11:62-74.

Chu, M., C.C. Gregorio, and C.T. Pappas. 2016. Nebulin, a multi-functional giant. *J Exp Biol*. 219:146-152.

Davy, D.A., H.D. Campbell, S. Fountain, D. de Jong, and M.F. Crouch. 2001. The flightless I protein colocalizes with actin- and microtubule-based structures in motile Swiss 3T3 fibroblasts: evidence for the involvement of PI 3-kinase and Ras-related small GTPases. *J Cell Sci*. 114:549-562.

de Winter, J.M., and C.A.C. Ottenheijm. 2017. Sarcomere Dysfunction in Nemaline Myopathy. *J Neuromuscul Dis*. 4:99-113.

Deak, II, P.R. Bellamy, M. Bienz, Y. Dubuis, E. Fenner, M. Gollin, A. Rahmi, T. Ramp, C.A. Reinhardt, and B. Cotton. 1982. Mutations affecting the indirect flight muscles of Drosophila melanogaster. *J Embryol Exp Morphol*. 69:61-81.

Deng, S., R.L. Silimon, M. Balakrishnan, I. Bothe, D. Juros, D.B. Soffar, and M.K. Baylies. 2021. The actin polymerization factor Diaphanous and the actin severing protein Flightless I collaborate to regulate sarcomere size. *Dev Biol*. 469:12-25.

Dlugosz, A.A., P.B. Antin, V.T. Nachmias, and H. Holtzer. 1984. The relationship between stress fiber-like structures and nascent myofibrils in cultured cardiac myocytes. *J Cell Biol*. 99:2268-2278.

Farkas, D., S. Szikora, A.S. Jijumon, T.F. Polgar, R. Patai, M.A. Toth, B. Bugyi, T. Gajdos, P. Biro, T. Novak, M. Erdelyi, and J. Mihaly. 2024. Peripheral thickening of the sarcomeres and pointed end elongation of the thin filaments are both promoted by SALS and its formin interaction partners. *Plos Genet*. 20:e1011117.

Fernandes, I., and F. Schock. 2014. The nebulin repeat protein Lasp regulates I-band architecture and filament spacing in myofibrils. *J Cell Biol*. 206:559-572.

Fletcher, D.A., and R.D. Mullins. 2010. Cell mechanics and the cytoskeleton. *Nature*. 463:485-492.

Fong, K.S.K., and H.G. de Couet. 1999. Novel proteins interacting with the leucine-rich repeat domain of human flightless-I identified by the yeast two-hybrid system. *Genomics*. 58:146-157.

Garg, A., J. O'Rourke, C. Long, J. Doering, G. Ravenscroft, S. Bezprozvannaya, B.R. Nelson, N. Beetz, L. Li, S. Chen, N.G. Laing, R.W. Grange, R. Bassel-Duby, and E.N. Olson. 2014. KLHL40 deficiency destabilizes thin filament proteins and promotes nemaline myopathy. *J Clin Invest*. 124:3529-3539.

Gonzalez-Morales, N., T.K. Holenka, and F. Schock. 2017. Filamin actin-binding and titin-binding fulfill distinct functions in Z-disc cohesion. *Plos Genet*. 13:e1006880.

Gonzalez-Morales, N., Y.S. Xiao, M.A. Schilling, O. Marescal, K.A. Liao, and F. Schock. 2019. Myofibril diameter is set by a finely tuned mechanism of protein oligomerization in Drosophila. *Elife*. 8.

Goshima, M., K. Kariya, Y. Yamawaki-Kataoka, T. Okada, M. Shibatohge, F. Shima, E. Fujimoto, and T. Kataoka. 1999. Characterization of a novel Ras-binding protein Ce-FLI-1 comprising leucine-rich repeats and gelsolin-like domains. *Biochem Biophys Res Commun*. 257:111-116.

Granato, M., F.J. van Eeden, U. Schach, T. Trowe, M. Brand, M. Furutani-Seiki, P. Haffter, M. Hammerschmidt, C.P. Heisenberg, Y.J. Jiang, D.A. Kane, R.N. Kelsh, M.C. Mullins, J. Odenthal, and C. Nusslein-Volhard. 1996. Genes controlling and mediating locomotion behavior of the zebrafish embryo and larva. *Development*. 123:399-413.

Granzier, H.L., and S. Labeit. 2005. Titin and its associated proteins: the third myofilament system of the sarcomere. *Advances in protein chemistry*. 71:89-119.

Guruharsha, K.G., J.F. Rual, B. Zhai, J. Mintseris, P. Vaidya, N. Vaidya, C. Beekman, C. Wong, D.Y. Rhee, O. Cenaj, E. McKillip, S. Shah, M. Stapleton, K.H. Wan, C. Yu, B. Parsa, J.W. Carlson, X. Chen, B. Kapadia, K. VijayRaghavan, S.P. Gygi, S.E. Celniker, R.A. Obar, and S. Artavanis-Tsakonas. 2011. A protein complex network of Drosophila melanogaster. *Cell*. 147:690-703.

Higashi, T., T. Ikeda, T. Murakami, R. Shirakawa, M. Kawato, K. Okawa, M. Furuse, T. Kimura, T. Kita, and H. Horiuchi. 2010. Flightless-I (Fli-I) regulates the actin assembly activity of

diaphanous-related formins (DRFs) Daam1 and mDia1 in cooperation with active Rho GTPase. *J Biol Chem*. 285:16231-16238.

Holtzer, H., T. Hijikata, Z.X. Lin, Z.Q. Zhang, S. Holtzer, F. Protasi, C. Franzini-Armstrong, and H.L. Sweeney. 1997. Independent assembly of 1.6 microns long bipolar MHC filaments and I-Z-I bodies. *Cell Struct Funct*. 22:83-93.

Hubner, N.C., A.W. Bird, J. Cox, B. Splettstoesser, P. Bandilla, I. Poser, A. Hyman, and M. Mann. 2010. Quantitative proteomics combined with BAC TransgeneOmics reveals in vivo protein interactions. *J Cell Biol*. 189:739-754.

Huxley, A.F., and R. Niedergerke. 1954. Structural changes in muscle during contraction; interference microscopy of living muscle fibres. *Nature*. 173:971-973.

Huxley, H.E., and W. Brown. 1967. The low-angle x-ray diagram of vertebrate striated muscle and its behaviour during contraction and rigor. *J Mol Biol*. 30:383-434.

Jani, K., and F. Schock. 2007. Zasp is required for the assembly of functional integrin adhesion sites. *J Cell Biol*. 179:1583-1597.

Katzemich, A., K.A. Liao, S. Czerniecki, and F. Schock. 2013. Alp/Enigma family proteins cooperate in Z-disc formation and myofibril assembly. *Plos Genet*. 9:e1003342.

Kooij, V., M.C. Viswanathan, D.I. Lee, P.P. Rainer, W. Schmidt, W.A. Kronert, S.E. Harding, D.A. Kass, S.I. Bernstein, J.E. Van Eyk, and A. Cammarato. 2016. Profilin modulates sarcomeric organization and mediates cardiomyocyte hypertrophy. *Cardiovascular research*. 110:238-248.

Kuwabara, Y., A.J. York, S.C. Lin, M.A. Sargent, K.M. Grimes, J.P. Pirruccello, and J.D. Molkentin. 2023. A human FLII gene variant alters sarcomeric actin thin filament length and predisposes to cardiomyopathy. *P Natl Acad Sci USA*. 120.

Labeit, S., and B. Kolmerer. 1995a. The complete primary structure of human nebulin and its correlation to muscle structure. *J Mol Biol*. 248:308-315.

Labeit, S., and B. Kolmerer. 1995b. Titins: giant proteins in charge of muscle ultrastructure and elasticity. *Science*. 270:293-296.

Lake, B.D., and J. Wilson. 1975. Zebra body myopathy. Clinical, histochemical and ultrastructural studies. *J Neurol Sci*. 24:437-446.

Lang, L., A. Pettko-Szandtner, H. Tuncay Elbasi, H. Takatsuka, Y. Nomoto, A. Zaki, S. Dorokhov, G. De Jaeger, D. Eeckhout, M. Ito, Z. Magyar, L. Bogre, M. Heese, and A. Schnittger. 2021. The DREAM complex represses growth in response to DNA damage in Arabidopsis. *Life Sci Alliance*. 4.

Lee, P.T., J. Zirin, O. Kanca, W.W. Lin, K.L. Schulze, D. Li-Kroeger, R. Tao, C. Devereaux, Y. Hu, V. Chung, Y. Fang, Y. He, H. Pan, M. Ge, Z. Zuo, B.E. Housden, S.E. Mohr, S. Yamamoto, R.W. Levis, A.C. Spradling, N. Perrimon, and H.J. Bellen. 2018. A gene-specific T2A-GAL4 library for Drosophila. *Elife*. 7.

Lemke, S.B., and F. Schnorrer. 2017. Mechanical forces during muscle development. *Mechanisms of development*. 144:92-101.

Lipinszki, Z., V. Vernyik, N. Farago, T. Sari, L.G. Puskas, F.R. Blattner, G. Posfai, and Z. Gyorfy. 2018. Enhancing the Translational Capacity of
by Resolving the Codon Bias. *Acs Synth Biol*. 7:2656-2664.

Lipov, A., S.J. Jurgens, F. Mazzarotto, M. Allouba, J.P. Pirruccello, Y. Aguib, M. Gennarelli, M.H. Yacoub, P.T. Ellinor, C.R. Bezzina, and R. Walsh. 2023. Exploring the complex spectrum of dominance and recessiveness in genetic cardiomyopathies. *Nat Cardiovasc Res*. 2:1078-+.

Littlefield, R., A. Almenar-Queralt, and V.M. Fowler. 2001. Actin dynamics at pointed ends regulates thin filament length in striated muscle. *Nat Cell Biol*. 3:544-551.

Littlefield, R.S., and V.M. Fowler. 2008. Thin filament length regulation in striated muscle sarcomeres: pointed-end dynamics go beyond a nebulin ruler. *Semin Cell Dev Biol*. 19:511-519.

Liu, Y.T., and H.L. Yin. 1998. Identification of the binding partners for flightless I, a novel protein bridging the Leucine-rich repeat and the gelsolin superfamilies. *Journal of Biological Chemistry*. 273:7920-7927.

Lu, M.H., C. DiLullo, T. Schultheiss, S. Holtzer, J.M. Murray, J. Choi, D.A. Fischman, and H. Holtzer. 1992. The vinculin/sarcomeric-alpha-actinin/alpha-actin nexus in cultured cardiac myocytes. *J Cell Biol*. 117:1007-1022.

Manisastry, S.M., K.J. Zaal, and R. Horowits. 2009. Myofibril assembly visualized by imaging N-RAP, alpha-actinin, and actin in living cardiomyocytes. *Exp Cell Res*. 315:2126-2139.

Mardahl-Dumesnil, M., and V.M. Fowler. 2001. Thin filaments elongate from their pointed ends during myofibril assembly in Drosophila indirect flight muscle. *J Cell Biol*. 155:1043-1053.

Menon, S.D., and W. Chia. 2001. Drosophila rolling pebbles: a multidomain protein required for myoblast fusion that recruits D-Titin in response to the myoblast attractant Dumbfounded. *Dev Cell*. 1:691-703.

Miklos, G.L., and H.G. De Couet. 1990. The mutations previously designated as flightless-I3, flightless-O2 and standby are members of the W-2 lethal complementation group at the base of the X-chromosome of Drosophila melanogaster. *J Neurogenet*. 6:133-151.

Mohammad, I., P.D. Arora, Y. Naghibzadeh, Y. Wang, J. Li, W. Mascarenhas, P.A. Janmey, J.F. Dawson, and C.A. McCulloch. 2012. Flightless I is a focal adhesion-associated actin-capping protein that regulates cell migration. *Faseb J*. 26:3260-3272.

Molnar, I., E. Migh, S. Szikora, T. Kalmar, A.G. Vegh, F. Deak, S. Barko, B. Bugyi, Z. Orfanos, J. Kovacs, G. Juhasz, G. Varo, M. Nyitrai, J. Sparrow, and J. Mihaly. 2014. DAAM Is Required for Thin Filament Formation and Sarcomerogenesis during Muscle Development in Drosophila. *Plos Genet*. 10.

Molodenskiy, D., V.J. Maurer, D. Yu, G. Chojnowski, S. Bienert, G. Tauriello, K. Gilep, T. Schwede, and J. Kosinski. 2025. AlphaPulldown2-a general pipeline for high-throughput structural modeling. *Bioinformatics*. 41.

Moncman, C.L., and K. Wang. 1996. Assembly of nebulin into the sarcomeres of avian skeletal muscle. *Cell Motil Cytoskeleton*. 34:167-184.

Naganawa, Y., and H. Hirata. 2011. Developmental transition of touch response from slow muscle-mediated coilings to fast muscle-mediated burst swimming in zebrafish. *Dev Biol*. 355:194-204.

Nagaoka, R., N. Minami, K. Hayakawa, H. Abe, and T. Obinata. 1996. Quantitative analysis of low molecular weight G-actin-binding proteins, cofilin, ADF and profilin, expressed in developing and degenerating chicken skeletal muscles. *J Muscle Res Cell Motil*. 17:463-473.

Neininger-Castro, A.C., J.B. Hayes, Z.C. Sanchez, N. Taneja, A.M. Fenix, S. Moparthi, S. Vassilopoulos, and D.T. Burnette. 2023. Independent regulation of Z-lines and M-lines during sarcomere assembly in cardiac myocytes revealed by the automatic image analysis software sarcApp. *Elife*. 12.

Nguyen, J.B., and Y. Modis. 2013. Crystal structure of the dimeric coiled-coil domain of the cytosolic nucleic acid sensor LRRFIP1. *Journal of Structural Biology*. 181:82-88.

Orfanos, Z., K. Leonard, C. Elliott, A. Katzemich, B. Bullard, and J. Sparrow. 2015. Sallimus and the dynamics of sarcomere assembly in Drosophila flight muscles. *J Mol Biol*. 427:2151-2158.

Orfanos, Z., and J.C. Sparrow. 2013. Myosin isoform switching during assembly of the Drosophila flight muscle thick filament lattice. *J Cell Sci*. 126:139-148.

Parker, F., T.G. Baboolal, and M. Peckham. 2020. Actin Mutations and Their Role in Disease. *Int J Mol Sci*. 21.

Passier, R., J.A. Richardson, and E.N. Olson. 2000. Oracle, a novel PDZ-LIM domain protein expressed in heart and skeletal muscle. *Mechanisms of development*. 92:277-284.

Perrimon, N., D. Smouse, and G.L. Miklos. 1989. Developmental genetics of loci at the base of the X chromosome of Drosophila melanogaster. *Genetics*. 121:313-331.

Pinter, R., T. Huber, P. Bukovics, P. Gaszler, A.T. Vig, M.A. Toth, G. Gazso-Gerhat, D. Farkas, E. Migh, J. Mihaly, and B. Bugyi. 2020. The Activities of the Gelsolin Homology Domains of Flightless-I in Actin Dynamics. *Front Mol Biosci*. 7:575077.

Pollard, T.D., and G.G. Borisy. 2003. Cellular motility driven by assembly and disassembly of actin filaments. *Cell*. 112:453-465.

Reedy, M.C., and C. Beall. 1993. Ultrastructure of developing flight muscle in Drosophila. I. Assembly of myofibrils. *Dev Biol*. 160:443-465.

Rees, E.J., M. Erdelyi, G.S.K. Schierle, A. Knight, and C.F. Kaminski. 2013. Elements of image processing in localization microscopy. *J Optics-Uk*. 15.

Rhee, D., J.M. Sanger, and J.W. Sanger. 1994. The premyofibril: evidence for its role in myofibrillogenesis. *Cell Motil Cytoskeleton*. 28:1-24.

Rhee, D.Y., D.Y. Cho, B. Zhai, M. Slattery, L. Ma, J. Mintseris, C.Y. Wong, K.P. White, S.E. Celniker, T.M. Przytycka, S.P. Gygi, R.A. Obar, and S. Artavanis-Tsakonas. 2014. Transcription factor networks in Drosophila melanogaster. *Cell reports*. 8:2031-2043.

Robinson, M.D., D.J. McCarthy, and G.K. Smyth. 2010. edgeR: a Bioconductor package for differential expression analysis of digital gene expression data. *Bioinformatics*. 26:139-140.

Roper, K., Y. Mao, and N.H. Brown. 2005. Contribution of sequence variation in Drosophila actins to their incorporation into actin-based structures in vivo. *J Cell Sci*. 118:3937-3948.

Ruijmbeek, C.W., F. Housley, H. Idrees, M.P. Housley, J. Pestel, L. Keller, J.K. Lai, H.C.V. der Linde, R. Willemsen, J. Piesker, Z.N. Al-Hassnan, A. Almesned, M. Dalinghaus, L.M.V. den Bersselaar, M.A. van Slegtenhorst, F. Tessadori, J. Bakkers, T.J. van Ham, D.Y. Stainier, J.M. Verhagen, and S. Reischauer. 2023. Biallelic variants in FLII cause pediatric cardiomyopathy by disrupting cardiomyocyte cell adhesion and myofibril organization. *JCI Insight*. 8.

Sanger, J.W., S. Kang, C.C. Siebrands, N. Freeman, A. Du, J. Wang, A.L. Stout, and J.M. Sanger. 2005. How to build a myofibril. *J Muscle Res Cell Motil*. 26:343-354.

Schafer, D.A., C. Hug, and J.A. Cooper. 1995. Inhibition of CapZ during myofibrillogenesis alters assembly of actin filaments. *J Cell Biol*. 128:61-70.

Schindelin, J., I. Arganda-Carreras, E. Frise, V. Kaynig, M. Longair, T. Pietzsch, S. Preibisch, C. Rueden, S. Saalfeld, B. Schmid, J.Y. Tinevez, D.J. White, V. Hartenstein, K. Eliceiri, P. Tomancak, and A. Cardona. 2012. Fiji: an open-source platform for biological-image analysis. *Nat Methods*. 9:676-682.

Schnorrer, F., C. Schonbauer, C.C.H. Langer, G. Dietzl, M. Novatchkova, K. Schernhuber, M. Fellner, A. Azaryan, M. Radolf, A. Stark, K. Keleman, and B.J. Dickson. 2010. Systematic genetic analysis of muscle morphogenesis and function in Drosophila. *Nature*. 464:287-291.

Shwartz, A., N. Dhanyasi, E.D. Schejter, and B. Shilo. 2016. The Drosophila formin Fhos is a primary mediator of sarcomeric thin-filament array assembly. *Elife*. 5.

Spletter, M.L., C. Barz, A. Yeroslaviz, X. Zhang, S.B. Lemke, A. Bonnard, E. Brunner, G. Cardone, K. Basler, B.H. Habermann, and F. Schnorrer. 2018. A transcriptomics resource reveals a transcriptional transition during ordered sarcomere morphogenesis in flight muscle. *Elife*. 7.

Squire, J.M., H.A. Al-Khayat, C. Knupp, and P.K. Luther. 2005. Molecular architecture in muscle contractile assemblies. *Advances in protein chemistry*. 71:17-87.

Stout, A.L., J. Wang, J.M. Sanger, and J.W. Sanger. 2008. Tracking changes in Z-band organization during myofibrillogenesis with FRET imaging. *Cell Motil Cytoskeleton*. 65:353-367.

Szikora, S., T. Gajdos, T. Novak, D. Farkas, I. Foldi, P. Lenart, M. Erdelyi, and J. Mihaly. 2020a. Nanoscopy reveals the layered organization of the sarcomeric H-zone and I-band complexes. *J Cell Biol*. 219.

Szikora, S., P. Gorog, and J. Mihaly. 2022. The Mechanisms of Thin Filament Assembly and Length Regulation in Muscles. *Int J Mol Sci*. 23.

Szikora, S., T. Novak, T. Gajdos, M. Erdelyi, and J. Mihaly. 2020b. Superresolution Microscopy of Drosophila Indirect Flight Muscle Sarcomeres. *Bio-protocol*. 10:e3654.

Trybus, K.M. 1994. Role of myosin light chains. *J Muscle Res Cell Motil*. 15:587-594.

Tsukada, T., C.T. Pappas, N. Moroz, P.B. Antin, A.S. Kostyukova, and C.C. Gregorio. 2010. Leiomodin-2 is an antagonist of tropomodulin-1 at the pointed end of the thin filaments in cardiac muscle. *J Cell Sci*. 123:3136-3145.

van de Linde, S., A. Loschberger, T. Klein, M. Heidbreder, S. Wolter, M. Heilemann, and M. Sauer. 2011. Direct stochastic optical reconstruction microscopy with standard fluorescent probes. *Nature protocols*. 6:991-1009.

Wang, K., J. McClure, and A. Tu. 1979. Titin: major myofibrillar components of striated muscle. *Proc Natl Acad Sci U S A*. 76:3698-3702.

Warrick, H.M., and J.A. Spudich. 1987. Myosin structure and function in cell motility. *Annu Rev Cell Biol*. 3:379-421.

Weitkunat, M., A. Kaya-Copur, S.W. Grill, and F. Schnorrer. 2014. Tension and force-resistant attachment are essential for myofibrillogenesis in Drosophila flight muscle. *Current biology : CB*. 24:705-716.

Yu, D., G. Chojnowski, M. Rosenthal, and J. Kosinski. 2023. AlphaPulldown-a python package for protein-protein interaction screens using AlphaFold-Multimer. *Bioinformatics*. 39.

Yuen, M., S.A. Sandaradura, J.J. Dowling, A.S. Kostyukova, N. Moroz, K.G. Quinlan, V.L. Lehtokari, G. Ravenscroft, E.J. Todd, O. Ceyhan-Birsoy, D.S. Gokhin, J. Maluenda, M. Lek, F. Nolent, C.T. Pappas, S.M. Novak, A. D'Amico, E. Malfatti, B.P. Thomas, S.B. Gabriel, N. Gupta, M.J. Daly, B. Ilkovski, P.J. Houweling, A.E. Davidson, L.C. Swanson, C.A. Brownstein, V.A. Gupta, L. Medne, P. Shannon, N. Martin, D.P. Bick, A. Flisberg, E. Holmberg, P. Van den Bergh, P. Lapunzina, L.B. Waddell, D.D. Sloboda, E. Bertini, D. Chitayat, W.R. Telfer, A. Laquerriere, C.C. Gregorio, C.A. Ottenheijm, C.G. Bonnemann, K. Pelin, A.H. Beggs, Y.K. Hayashi, N.B. Romero, N.G. Laing, I. Nishino, C. Wallgren-Pettersson, J. Melki, V.M. Fowler, D.G. MacArthur, K.N. North, and N.F. Clarke. 2014. Leiomodin-3 dysfunction results in thin filament disorganization and nemaline myopathy. *J Clin Invest*. 124:4693-4708.

Zhao, B., K. Zhang, C.S. Chen, and E. Lejeune. 2021. Sarc-Graph: Automated segmentation, tracking, and analysis of sarcomeres in hiPSC-derived cardiomyocytes. *PLoS Comput Biol*. 17:e1009443.

Zhou, Q., P. Ruiz-Lozano, M.E. Martone, and J. Chen. 1999. Cypher, a striated muscle-restricted PDZ and LIM domain-containing protein, binds to alpha-actinin-2 and protein kinase C. *J Biol Chem*. 274:19807-19813.